Fast adaptation of Myosin II activity to confinement sustains neutrophil migration in capillaries.

Mathieu Deygas1,2*; Mathilde Bernard1,2†; Pierre Nivoit3†; Lucie Barbier1,5; Li Wang1; Mathieu Maurin4; Emmanuel Tejerina2; Theresa Jakuszeit1; Alexandre Deslys2; Moira Garcia-Gomez2; Oumaima Baaziz2; Serge Garbay2; Emmanuel Terriac1,6; Rafaele Attia1,7; Guillaume Duménil3; Matthieu Piel1*; Pablo Vargas1,2*.

AFFILIATIONS:

1. Institut Curie and Institut Pierre-Gilles de Gennes, PSL Research University, CNRS, UMR 144, F-75005, Paris, France.
2. Leukomotion Lab, Paris Cité University, INSERM UMR-S1151, CNRS UMR-S8253, Institut Necker Enfants Malades, F-75015 Paris, France.
3. Institut Pasteur, Université Paris Cité, INSERM UMR1225, Pathogenesis of vascular infections, F-75015 Paris, France
4. Institut Curie, PSL Research University, CNRS, U932, F-75005, Paris, France.
5. Current address: Center for Interdisciplinary Research in Biology (CIRB), Collège de France, CNRS, INSERM, Université PSL, Paris, France.
6. Current address. Cell Polarity, Migration and Cancer Unit, Institut Pasteur, UMR3691 CNRS, Equipe Labellisée Ligue Contre le Cancer, F-75015 Paris, France.
7. Current address. Developmental biology laboratory, Sorbonne Université, CNRS UMR7622

†These authors contributed equally to this work.
*Corresponding authors: M.D: mathieu.deygas@inserm.fr; M.P: matthieu.piel@curie.fr; P.V: pablo.vargas@inserm.fr

ABSTRACT

As the first responders of the immune system, neutrophils rapidly reach inflamed tissues within minutes, navigating the intricate network of blood capillaries. Therefore, their ability to effectively control infections hinges on their capacity to squeeze and migrate through the micrometric tubes that drain the affected area. To understand this process, we investigated neutrophil migration in capillary tubes. *In vivo*, we observed that neutrophil crawling at the site of infection was largely independent of the size of the capillaries they traversed. Detailed *in vitro* studies showed that these cells could dynamically sustain their motility in microenvironments imposing confinement changes. Notably, other leukocytes failed to adapt their migration speed to these confinement levels. Mechanistically, neutrophils dynamically adapted their actomyosin cytoskeleton to confinement within seconds, a process essential to sustain their speed in capillaries of varying diameters. These cytoskeleton changes were reversible and correlated with the degree of confinement. Importantly, we observed cytoskeleton adaptation to confinement in capillaries *in vivo*. These findings reveal a unique mechanism that enables neutrophils to maintain their speed in blood capillaries, potentially contributing to the efficacy of innate immune reactions.

INTRODUCTION

Neutrophils are the most abundant immune cells in circulation. They are the first line of defense against infections, acting as rapid responders to threats[1]. These cells are among the fastest migrating in the body, reaching speeds of up to 30 μm/min in tissues – significantly faster than other migratory cells[2,3]. Their remarkable speed and plasticity are crucial for their effective immune responses in a broad range of microenvironments[4]. However, excessive neutrophil recruitment to tissues can lead to organ dysfunction[5]. Therefore, neutrophil recruitment and retention in tissues is tightly controlled.

In the last years, it has become clear that neutrophils have developed specific adaptations to facilitate their deformation and movement in confined spaces. For instance, neutrophils lack LaminA/C expression, which has been proposed to decrease nuclear stiffness and thus facilitate its deformation and migration[6]. In the same line, chemokine signaling can additionally trigger nuclear compaction, boosting neutrophil migration under confinement[7]. Moreover, neutrophils have specific mechanisms to prevent cellular crowding and limit potential tissue damage. For instance, while migrating in tubular networks *in vitro*, they avoid dead-ends by sensing microenvironmental pressure, a process known as barotaxis[8]. *In vivo*, neutrophils avoid their accumulation in the same capillary by diverting from other cells blocking the vessels[9]. Apart from mechanical cues, the biochemical properties of inflamed tissues, as hypoxia, modulate neutrophil motility in tubular structures[10]. This evidence highlights that neutrophils use multiple strategies to ensure their motility toward the core of the inflammation site.

Despite growing evidence on the regulation of neutrophil motility, it is still unclear how these cells adapt their migration to the structural irregularities of the tissue microenvironment. Due to their elevated speed, these cells would pass through multiple tissue compartments in a few minutes during inflammation, implying that they rapidly overcome variations of confinement *in vivo*. While microenvironment physical irregularities can steer neutrophil migration in low-adhesion conditions[11], how neutrophil respond and adapt to confinement remains to be investigated.

At initial phases of inflammation, neutrophils reach the inflamed tissues through the blood capillaries. Depending on the organ, these capillary networks show different organization and variable diameter (~2-15 μm)[12–14]. This might impose transient or continuous physical confinement to cells, consistently with reports showing neutrophil migration in capillaries with a lumen smaller than the cell diameter in various inflamed tissues[12,15–17]. In such capillaries,

neutrophils have been shown to crawl actively, independently of blood flow[15–17]. This migration must be fine-tuned since neutrophil obstruction of capillary tubes might cause microvascular dysfunction, resulting in stroke and contributing to Alzheimer's disease[13,18–20]. In this context, it is critical to better understand the cellular mechanisms underlying neutrophil migration in confining blood capillaries.

In this work, we investigated neutrophil migration in capillaries *in vivo* and *in vitro*. We showed that, in both systems, neutrophil migration speed was independent of the capillary diameter. Additionally, we showed that these cells could adapt their migration speed to confinement changes in seconds. This phenomenon was specific to neutrophils, since other leukocytes failed to sustain their speed under strong confinement. Mechanistically, neutrophil migration relied on the rapid and reversible reorganization of the actomyosin cytoskeleton in response to confinement. This work reveals that a cell intrinsic adaptation of cell contractility to confinement, which drives neutrophil migration in blood capillaries under strong confinement.

RESULTS

Neutrophil crawling in blood capillaries is independent of confinement levels

We first investigated neutrophil migration in blood capillaries *in vivo.* For that, we performed subcutaneous live cell imaging of endogenous neutrophils in the mouse flank skin system. In its blood capillary network, neutrophil crawling may occur independently of the blood flow, as being previously reported[15]. Imaging of this capillary network revealed a parallel array of tubes with diameters ranging between 3 and 9 µm (median = 3.6 µm) (Figure 1a-1c). In the absence of tissue inflammation, neutrophils were barely detected (Figure 1a). Local infection with *Neisseria meningitidis* (*Nm*) triggered neutrophil recruitment, which we observed 1-hour post-infection (Figure 1a). As expected, these cells subsequentially extravasated and accumulated in the infected tissue over the course of infection (Supplementary Fig. 1a-c).

Morphometric analysis of neutrophils within the capillaries 1-hour post-infection evidenced a wide range of confinement-induced cell deformations, as measured by the cell aspect ratio (AR, cell length divided by cell width) (Figure 1d-1g). While some neutrophils were almost round, others were ten times longer than wide, with an average AR of 6 (Figure 1e-1g, Supplementary Figure 1d). Analysis of neutrophil migration in capillaries using live-cell imaging showed that 40% of cells were crawling (speed < 50 µm/min, average speed 22 µm/min), 20% were flowing (speed > 50 µm/min), and 40% alternated between flowing and crawling phases (Figure 1h-i, Supplementary Figure 1e-g,). We observed some crawling neutrophils changing direction within the tubes or migrating against blood flow, which reflected their active migration (Supplementary Figure 1h). Strikingly, the instantaneous speed of crawling neutrophils did not depend on the extent of cell deformation (Figure 1k). These findings show that endogenous neutrophil crawling in blood capillaries is independent of the tube diameter, indicating that capillary-induced cell confinement does not restrict neutrophil migration *in vivo*.

Neutrophils maintain their speed in microchannels of different sizes independently of cell adhesion

The results obtained *in vivo* cannot rule out the potential contribution of microenvironmental biochemical factors in sustaining neutrophil migration in blood capillaries. To isolate the effect of physical constraints on neutrophil crawling, we took advantage of microfabricated channels with different cross-section areas (from 3 to 8 µm width, 4 µm height), which reproduced the diameter

range of the flank skin blood capillaries *in vivo* (Figure 2a). As a cellular model, we used primary GM-CSF treated bone-marrow neutrophils (mNeu)[7,10], which exhibited a phenotypic profile resembling matured neutrophils (Supplementary Figure 7)[21]. In terms of motility, mNeu entered spontaneously into fibronectin-coated microchannels of all dimensions tested, in the absence of any chemoattractant (Figure 2a-2f, Supplementary Figure 2). Morphometric analysis of neutrophils migrating in these microchannels showed that cell elongation increased with the confinement level. Indeed, the average cell AR ranged from 2.3 in 8 µm-width microchannels to 9.3 in 3 µm-width microchannels (Figure 2c). These values are within the range of *in vivo* measurements (Figure 1f). The nucleus AR also increased as a function of the confinement level, indicating full cell deformation (Supplementary Figure 2b). Single-cell migration analysis of mNeu revealed an average speed equivalent across all microchannels sizes (around 17 µm/min) (Figure 2d-2f,). Similarly to *in vivo* data, cell migration speed in microchannels of different sizes did not correlate with the cell AR (Figure 2e). This data show that spontaneous mNeu migration is not impacted by the confinement imposed by the microchannels.

Then, we investigated whether cell adhesion could affect neutrophil migration under confinement. First, we repeated the experiment using microchannels of different widths, but we coated them with either collagen or ICAM-1 adhesion molecules. As previously observed with fibronectin coating, mNeu exhibited the same speed in the different confinements (Figure 1f). Second, we passivated the microchannels surface with PLL-PEG or Pluronic F-127 to eliminate specific adhesion signaling. mNeu average speed was still independent of the confinement level despite being lower than in the presence of adhesion molecules (Figure 1f). These data suggest that mNeu can maintain their speed at different confinement levels in an adhesion-independent manner.

Neutrophils adapt their motility to confinement

We then investigated whether neutrophils could adapt their migration to confinement changes, as observed *in vivo* (Supplementary Figure 1a) First, we assessed mNeu migration in microchannels imposing a sharp decrease in their width from 6 to 3 µm (constant heigh of 4 µm) (Figure 3a). As expected, entry in the small section led to an increase in the cell aspect ratio (Figure 3a and Supplementary Figure 3b). However, despite strong cell elongation, mNeu maintained their average speed when passing from the wide to the narrow channel section (Figure 3b-3c). At the single cell level, the speed ratio was close to one, indicating that mNeu adapted their speed during

this transition (Figure 3d). In this system, 50% of the cells passed the transition in less than 2 min (Figure 3e and Supplementary Figure 3c) and 95% had passed in less than 6 min (Supplementary Figure 3c). Experiments in which mNeu migrated from narrow to wide channel sections also showed speed maintenance (Supplementary Figure 3d-f) and all cells passed the transition in less than 5 min (Supplementary Figure 3g). We then addressed whether neutrophil migration adaptation was reversible. For that, we used microchannels alternating successive 6 µm and 3 µm wide sections (Figure 3f). Notably, mNeu average speed and crossing time were unchanged in each transition (Figure 3g-h and Supplementary Figure 3h). These data show that neutrophils can adapt their migration to confinement changes in an *in vitro* capillary system, and that this adaptation is reversible. It also indicates lack of confinement memory in neutrophil migration in this system.

We then investigated neutrophil adaptation to gradual changes in confinement. For that, we investigated mNeu motility in funnel-shaped microchannels decreasing their width from 8 µm to 2 µm over 300 µm or 600 µm (Figure 3i). Morphological analysis showed gradual increase in cell aspect ratio as the mNeu migrated from the wide to the narrow side of the funnel (Figure 3j and supplementary Figure 3i-j). Notably, the cell speed remained constant despite the confinement increase, either over 300 µm or 600 µm (Figure 3j and supplementary Figure 3i-j). This data shows that cell speed maintenance is not altered by the intensity of the microchannel diameter reduction.

We then investigated whether speed maintenance under confinement was specific to neutrophils. For that, we assessed the capacity of other primary leukocytes to migrate from loose to confined microchannels. Notably, immature dendritic cells (iDCs), T lymphocytes (TLs) and Natural killer (NK) cells were unable to sustain their motility when transiting from the loose to the confined microchannel section, despite increase in cell elongation (Figure 3k). Single-cell speed measurements showed that the three cell types showed a drastic decrease (60%, 40% and 50% for iDCs, TLs and NKs, respectively) in their speed when passing to the confined microchannel section (Figure 3l).

Altogether, these data demonstrate that primary neutrophils have a cell-intrinsic capacity to maintain their motility upon confinement changes imposed by a capillary tube *in vitro*. The speed maintenance is reversible, and is also observed in funnel-shaped microchannels, indicating that neutrophils can adapt their migration to abrupt or gradual changes in the degree of confinement.

This speed maintenance seems specific to neutrophils, since other leukocytes fail to sustain speed upon change in confinement level.

F-actin polarity is regulated by confinement level

The ameboid motility of neutrophils and other leukocytes relies on actomyosin contractility, responsible of generating the force that pushes the cell body forward under confinement[22]. We thus analyzed F-actin remodeling during neutrophil passage from loose to narrow microchannel sections (Figure 4a). Confocal live cell imaging of Lifeact-EGFP expressing mNeu showed cortical actin distribution in the wide section of the microchannel, with a preferential accumulation at the cell front, as described previously for neutrophil like-cells[23]. Notably, passage to the narrow section was accompanied by fast F-actin accumulation at the cell rear (Figure 4a-c and Supplementary Figure 4a-b). Mapping the average F-actin signal during mNeu migration in each microchannel section confirmed a front-to-back F-actin transition (Figure 4c). To classify the cells based on F-actin positioning, we used the back-to-front actin ratio (BFAR) as metric (Figure 4d). This indicator was lower than 1 in 6 µm microchannels and increased above 1 upon cell passage to the narrow section, indicating a front-to-back switch (Figure 4e). Spatial analysis showed that BFAR changed concomitantly with cell elongation, without change in cell speed (Figure 4f and Supplementary Figure 4c). Analysis at the single-cell-level showed a positive correlation between BFAR and speed ratios (Figure 4g). This indicates that the migratory behavior of neutrophils in the size-transition channel is directly associated with the redistribution of F-actin at the cell rear. Of note, cells incapable of concentrating F-actin at the cell rear fail to adapt their speed to compression (Supplementary Figure 4d). In agreement with cell adaptation to confinement, F-actin went back to the front when cells passed from the 3 µm to the 6 µm microchannel section (Supplementary Figure 4e). This shows rapid and reversible F-actin reorganization in response to confinement in these cells.

To get better insight on the sensitivity of the F-actin to confinement, we mapped average F-actin signal in mNeu migrating in microchannels of different sizes (8 µm to 3 µm, as previously shown). In the range of 8 µm to 6 µm width, F-actin accumulated at the cell front (Figure 4h-j and Supplementary Figure 4f). Then, in the range from 5 µm to 3 µm, cells became more elongated, and F-actin gradually accumulated at the cell rear (Figure 4h-j and Supplementary Figure 4f). The fraction of cells with average F-actin at the rear also increased with confinement (Figure 4k).

Notably, speed and BFAR showed a positive correlation in microchannels of different widths at the instantaneous or cell average level (Figure 4l and Supplementary Figure 4g). This indicates that the F-actin accumulation at the rear associates to fast migration phases at any confinement level. Moreover, as confinement increases, cells exhibited a higher F-actin enrichment to reach a given speed.

Overall, these data demonstrate that actin cytoskeleton is rearranged dynamically, in a timescale of seconds, in response to change in confinement level during neutrophil migration. This actin polarity shift seems required for their speed maintenance.

Myosin II is activated by confinement and required for neutrophil speed maintenance

We next investigated Myosin II (MyoII) activation under confinement. For that, we performed immunofluorescence of active MyoII (pMLC2) in neutrophils migrating from 6 µm to 3 µm width microchannels. The results showed higher pMLC2 staining in the confined section, indicating increased contractility under confinement (Figure 5a-b, Supplementary Figure 5a). We then analyzed MyoII dynamics taking advantage of primary neutrophils obtained from MyoII-GFP mice[24]. Spinning disk live-cell imaging showed MyoII-GFP distribution all over the cell body, with cortical puncta and diffuse cytoplasmic sub-localizations (Figure 5c). Upon cell passage to the narrow section of the microchannel, overall MyoII-GFP signal concentrated in the cortex at the cell rear (Figure 5c). We concentrated our analysis in the cortical MyoII-GFP signal since it has been used as a proxy for its contractile activity (Figure 5d)[25–27]. Dynamic measurement showed almost instantaneous increase in cortical MyoII-GFP upon neutrophil entry in the 3 µm width microchannel (Figure 5c-e). Cortical MyoII-GFP at the cell rear was detected before full cell elongation in the confined microchannel, evidenced by a faster increase as compared to the cell aspect ratio (Figure 5e). Altogether, this data shows fast MyoII activation at the cortex of the cell rear upon neutrophil entry in a confined microchannel.

We then investigated the role of MyoII in neutrophil migration adaptation to confinement. Inhibition of the ATPase activity of MyoII using blebbistatin (BBS) decreased neutrophil migration in both microchannels sections. However, BBS had a bigger effect on the more confined area of the microchannel (Figure 5f). In agreement, single-cell analysis of the speed ratio between both sections showed a decrease upon BBS treatment, indicative of defective migration adaptation to confinement (Figure 5g). Similar results were observed upon Rho kinase (ROCK) inhibition

(Y-27632), one of the pathways responsible for MyoII activation (Figure 5f-g and Supplementary Figure 5b)[28]. Consistently, the time taken by neutrophils to pass to the confined section of the microchannel increased upon ROCK inhibition (Figure 5h-i). However, no effect was detected upon MLC kinase (MLCK) inhibition (ML-7), a kinase that regulate MLC levels (Figure 5g and Supplementary Figure 5c).

Then, we investigated the role of calcium on neutrophil migration adaptation to confinement. Strikingly, neutrophil passage to the confined section of the microchannel triggered cytosolic calcium increase, evidenced by calcium pulsations (Supplementary Figure 5d). However, treatment to deplete extracellular (EGTA) or intracellular (BAPTA-AM) calcium stores did not affect neutrophil ability to adapt their migration to confinement (Supplementary Figure 5e). Additionally, inhibition of transient receptor potential (TRP) channels (ACA) and cationic mechanosensitive channels (GsMTx4), including Piezo, did not affect their migration adaptation (Supplementary Figure 5e). This data shows that neutrophil adaptation to confinement occurs through cell contractility activated independently of mechanosensitive calcium signaling.

Then, we characterized the impact of ROCK inhibition on the dynamics of neutrophil adaptation to confinement. Spatial evolution of mNeu relative speed showed that ROCK inhibited cells slowed down as compared to control cells during passage from the 6 µm to 3µm microchannel section (Figure 5i-j). ROCK inhibition also affected F-actin dynamics, limiting accumulation at the cell rear upon passage in the small microchannel (Figure 5i,k). This result was confirmed by mapping average F-actin signal in both sections of the microchannel, in which ROCK inhibition lowered signal concentration at the cell rear (Figure 5l). Furthermore, analysis of F-actin distribution in response to confinement using microchannels of different sizes showed that ROCK inhibition effect on F-actin was observed in all microchannel sizes and prevented F-actin enrichment at the rear as confinement level increases (Figure 5m).

Altogether, this data indicates that fast confinement-induced ROCK-dependent MyoII activation at the cell rear is required for neutrophil migration adaptation to confinement in MLCK and calcium independent manner.

Neutrophils adapt cell migration and actin cytoskeleton to confinement *in vivo.*

We finally addressed whether actomyosin rearrangements occur during neutrophils migration in capillaries *in vivo*. For that, we injected Lifeact-EGFP expressing neutrophils in wild type recipient

mice to visualize F-actin rearrangements in skin blood capillaries. Intravital spinning-disk live cell imaging showed preferential Lifeact-EGFP signal at the cell rear in most capillaries (Figure 6a-b). This is equivalent to the F-actin distribution observed in 3µm width microchannels, in which cells showed similar aspect ratio than skin capillaries (Figure 1f-g, and 2c). However, since most skin capillaries were homogeneous in diameter, we could not image F-actin dynamic adaptation.
Thus, we imaged neutrophil migration in another tissue model, the liver sinusoids (Figure 6c)[17]. In this system, the capillaries have a higher average diameter and broader distribution as compared to skin capillaries (Figure 6d). Consequently, neutrophils exhibited a lower cell aspect ratio in the liver sinusoids (Figure 6e). The average neutrophil speed in the sinusoids was around 10 µm per min (Figure 5f). These cells showed F-actin concentration mostly at the cell front (Figure 6g). This is consistent with F-actin distribution observed in 6 µm width microchannels, in which neutrophils exhibit similar aspect ratio (Figure 2c and 6e). In this tissue we could image neutrophils migrating from a wide to a narrow section of the capillaries. Notably, F-Actin accumulated at the cell rear upon passage in the narrow section of the capillary (Figure 6h). This indicates that the neutrophil actin cytoskeleton can adapt to confinement *in vivo*. We further correlated actin positioning to cell speed in cells crawling in the skin and liver capillaries. We observed a positive correlation between F-actin positioning and cell speed in both systems. Nonetheless, F-actin positioning at the cell rear was higher in the skin capillaries (Figure 6i). This is in agreement with *in vitro* data in microchannels of different sizes (Supplementary Figure 4g). Overall, we show that F-actin distribution at the cell rear correlates positively with neutrophil speed in capillaries *in vivo*. This indicates that neutrophils have the cell intrinsic capacity to sense the degree of confinement, which seems to be independent of the tissue.

DISCUSSION

By combining *in vivo* imaging and *in vitro* microfabricated devices, we have established that neutrophil actomyosin cytoskeleton adapts dynamically to the confinement level during their crawling in capillaries. This adaptation relies on the rapid activation of MyoII at the cell rear under strong confinement, which is controlled by ROCK activity. This mechanism allows a cell autonomous capacity of neutrophils to maintain a fast motility despite strong cell deformations *in vitro* and *in vivo*.

Neutrophil migration in capillaries *in vivo*

Exploring the mouse microvasculature, we revealed that neutrophils maintain a fast-crawling capacity despite strong cell elongation in confining capillaries in the skin and the liver. In the skin, which displays very thin capillaries, the neutrophils capacity to sustain a fast motility might be important to avoid "traffic jam" by massive retention of neutrophils in the tubes, preventing tissue perfusion and inducing tissue damage[9]. However, the role of neutrophil crawling in confining capillaries in the context of local skin infection remains difficult to tackle[15]. The neutrophil capacity to sustain speed under confinement is also observed in the liver sinusoids, where we show that neutrophil speed is maintained upon changes in confinement. Although the liver exhibits shorter and less frequent confining sinusoids than skin capillaries, their diameter can decrease drastically upon sterile injury, where neutrophils are massively recruited for tissue healing[3]. Our work also emphasizes that neutrophils can adapt their migration machinery upon deformation *in vivo* in seconds. This capacity might prevent circulating neutrophils from being trapped when facing abrupt reduction of capillary diameter. Interestingly, single neutrophils were found stuck in brain capillaries, causing perfusion disfunction in Alzheimer disease or after ischemic stroke [13,19,20].

Study of neutrophil migration using *in vitro* capillaries

Confined cell crawling in capillaries *in vivo* is technically challenging, limiting the number of experiences that can be performed. In addition, it is not possible to dissociate the confinement induced by capillaries from specific tissue properties, such as inflammatory molecules, adhesion molecules and blood flow. Therefore, we used *in vitro* microfabricated tubes to mimic the shape of *in vivo* capillaries and study specific aspects of neutrophil migration.

In our setup of microfabricated capillaries, neutrophils migrate spontaneously, in the absence of flow. Taking advantage of *in vitro* capillaries of different sizes, we were able to demonstrate that

neutrophils have the same speed, independently of the confinement level. Notably, we showed that neutrophil speed maintenance did not rely on specific cell adhesions. Whilst the basal speed of neutrophils is influenced by the type of molecule present on the surface of the microchannels, their ability to sustain this speed under varying degrees of confinement remains unchanged. This might partially explain our observation that basal neutrophil migration speed in the skin capillaries doubled that of the liver sinusoids. Nevertheless, neutrophils showed migration adaptation to confinement in both systems, indicating that the migratory response to confinement in a capillary system can be dissociated from cell adhesions *in vitro* and *in vivo*.

Neutrophil migration adaptation to confinement changes

Being aware that *in vivo* situations are related to variations in the microenvironment, we took advantage of microfabrication to impose confinement changes to neutrophils migrating in capillaries. Notably, neutrophils were able to accommodate their speed when facing an abrupt reduction or increase in the diameter of the tubes, or when facing gradual changes in confinement. It has been already proposed that in irregular microenvironments, leukocytes can tune their motility to avoid high resistance from their microenvironment[8,29,30]. However, in our system cells are forced to face confinement. Notably, 95% of the neutrophils go in the confined area of the microchannel, showing their capacity to bypass confinement. Interestingly, other leukocytes tested did not adapt their migration to a sharp reduction in the confinement level. This can be related to a size issue in immature dendritic cells, bigger than neutrophils, situation that might difficult cell deformation. However, TLs and NK cells have a similar size as compared to neutrophils, and they still do not maintain their speed upon confinement. It remains to be determined if this is the same for other leukocytes. For instance, we have shown that activated dendritic cells have similar speed at different confinement levels[31]. This indicates that cell migration adaptation to confinement might be related to the function and activation state of the leukocyte[32,33]. It can also relate to differences in nuclear stiffness, since laminA/C expression differs between immune cells and affects neutrophil-like cell passage through micron-scale constrictions[34,35].

Cytoskeleton adaptation of neutrophil migration machinery to confinement

By combining *in vivo* and *in vitro* experiments, we revealed that the neutrophil actomyosin cytoskeleton distribution depends on capillaries cross sections area. In capillaries wider than 6 µm neutrophils accumulated actomyosin mostly at the cell front, while in capillaries narrower than 5 µm, these cells accumulated actomyosin mostly at their back. In leukocytes, such actomyosin

plasticity underlying cell migration has already been evidenced upon cell activation[36] or upon genetic or pharmacological perturbations[37,38]. Our work stresses that the actomyosin organization may be dictated by the microenvironment physical properties, thus ensuring neutrophil motility in confining capillaries.

Moreover, we also showed that neutrophil instantaneous speed positively correlates with higher F-actin enrichment at the cell back for a given cross-section area. This result is consistent with previous studies correlating leukocyte speed to actomyosin intracellular localization[36,36,39–43]. This result is also in agreement with increased cell speed upon front F-actin depletion in walker carcinoma cells and dendritic cells[36–38]. In addition, we showed that, to reach a given speed, enrichment of F-actin at the neutrophil back becomes critical as the confinement increases. This highlights a specific neutrophil adaptation to generate the forces required to circumvent high resistance[44,45]. We also evidenced that such cell adaptations to confinement rely on MyoII activity in neutrophils, corroborating previous studies in other cell types[31,32,46–48].

Fast neutrophil migration adaptation to confinement through MyoII activation

We showed that the MyoII activation was critical to ensure fast neutrophil migration upon confinement. This is in agreement with a recent study in NK cells showing MyoII-dependent cell contraction upon cell deformation in 3D microenvironments[49]. Additionally, MyoII activation upon confinement has been evidenced in other cell types[25–27,50]. In such systems, MyoII activity increased seconds upon cell confinement in a calcium-dependent manner. However, in our study, we showed that MyoII activation in neutrophils was independent of calcium signaling but relied on the activation of the ROCK pathway. The upstream signaling is still under investigation, but it might be related to cell deformation itself. For example, GEF-H1 release from microtubules might activate MyoII upon cell confinement[51,52]. In addition, it has been proposed that membrane proximity upon cell deformation can concentrate signaling molecules and lead to signaling pathway regulation[53].

To conclude, this work shows that fast, dynamic and reversible actomyosin organization in neutrophils drives their fast migration in capillaries, independently of the confinement they impose on these cells. This cell autonomous mechanisms may prevent neutrophils jamming upon and tissue damage upon inflammation

AUTHOR CONTRIBUTIONS:

M.D. performed and analyzed most experiments. M.B. analyzed data of *in vitro* experiments. P.N. performed the *in vivo* experiments. M.M. wrote ImageJ macros for image processing and analysis L.B., performed experiments with immature dendritic cells; L.W. performed photolithography; T.J. helped with image analysis; E.T. performed FACS analysis; O.B. performed TL experiments; A.D. helped with image processing and analysis; S.G. helped with analysis; M.G.G. performed NK experiments; E.T. and R.A. did initial experiments with dendritic cells; G.D. supervised *in vivo* experiments; M.D., M.P., and P.V., designed the study. M.D. and P.V. wrote the initial version of the manuscript with M.P. insights. All authors contributed to discussions and the final version of the manuscript.

ACKNOWLEDGEMENTS:

We thank Ana-Maria Lennon Duménil (Institut Curie, Paris, France) and Fernando Sepulveda (Institut Imagine, Paris, France) for sharing mice stocks. We thank Matthieu Bernard for helping with raw data processing from Metamorph. We thank the animal facility at the Institut Curie, and the microscopy facility of IPGG for equipment and technical assistance.

FUNDING:

This work was supported by The French National Institutes of Health and Medical Research (INSERM). This work received funding of the Association Nationale pour la Recherche (ANR-16-CE13-0009, ANR-22-CE15-0041, ANR-21-CE17-0050); Labex IPGG; IdEx Université de Paris « Chaires nouvelles équipes » (P.V.). FRM postdoc fellowship (SPF201809007121) (M.D.); Labex IBEID (ANR 10-LBX-62 IBEID) (G.D.); Fondation ARC pour la recherche sur le cancer (grant n°ARCDOC42023010006205) (M.B.); FRM team EQU202103012677 (M.P.) and the support of "Institut Pierre-Gilles de Gennes" (laboratoire d'excellence, "Investissements d'avenir" program ANR-10-IDEX-0001-02 PSL and ANR-10-LABX-31).

FIGURE LEGENDS:

Figure 1:

a. Spinning disc-confocal images of subcutaneous blood capillaries (gray, fluorescent BSA) and endogenous neutrophils (orange, Ly6G) at steady state (left) and two hours after *N.meningitidis* infection (right). Neutrophils located inside capillaries are indicated with white arrow. Scale bar: 20 µm. b. Magnifications of three capillary segments revealed by fluorescent BSA. Scale bar: 5 µm. c. Frequency distribution (percentage) of subcutaneous capillary diameters. Data are pooled from two independent experiments, for a total of 90 segments. d. Magnification of two cells trafficking inside the microvasculature. Scale bar: 5 µm. e. Montage of 30 cells trafficking in subcutaneous capillaries, pseudo-colored by the value of their aspect ratio. f. Frequency distribution of cell aspect ratio of neutrophils trafficking inside capillaries. n=740 shapes from 3 independent experiments. g. Mean cell aspect ratio of 61 cells from 3 independent experiments. h. Percentage of flowing, crawling and intermittently flowing and crawling cells inside subcutaneous capillaries from 3 independent experiments (total of 229 cells). h. Migration speed of individual crawling cells in subcutaneous capillaries, n = 61 cells from 3 independent experiments. i. Kymographs of two neutrophils crawling in subcutaneous capillaries of different diameters. Cell aspect ratio is represented in pseudo color corresponding to the legend in fig 1f. j. Scatter plots comparing instantaneous speed and instantaneous cell aspect ratio of crawling cells in subcutaneous capillaries. n = 679 timepoints from 61 cells from 3 independent experiments. Spearman correlation coefficient = 0.09, P = 0.017 (two tailed).

Figure 2:

a: Examples of *in vivo* neutrophils in subcutaneous capillaries (left) and *in vitro* bone-marrow neutrophils in microchannels of different widths (right). Scale bar 5 µm. b: Cross sections of Lifeact-EGFP expressing neutrophils (left) and representation of 30 cell contours (sum) per channel width (top view, right). c: Distribution of mean cell aspect ratio, from 3 independent experiments. Median +/- SD is indicated for each channel width. 8um, n= 183; 7um, n = 150; 6um, n = 205; 5 um, n = 218; 4 um, n = 231; 3 um, n = 214. d: Distribution of mean cell speed. Data are pooled from 5 independent experiments. Median +/- SD is indicated for each channel width. 8um, n= 289; 7um, n = 263; 6um, n = 333; 5 um, n = 314; 4 um, n = 345, 3 um, n = 350. e: Cell

aspect ratio correlation to cell speed of neutrophils. Dots, individual cell shape/speed value of neutrophils in 7, 5 and 3 um channel width. Data are representative of 3 independent experiments. 7 um, n = 2189; 5 um, n = 2876; 3 um, n = 2137. Spearman correlation coefficient = 0.02, P = 0.056 (two-tailed). f: Mean cell speeds of neutrophils migrating in microchannels of 7, 5, 3 um widths coated with different surface molecules, from 2 or 3 independent experiments. Median of each experiment are represented by paired bigger dots. Fibronectin 10µg/ml, 7 um, n = 277; 5 um, n = 209; 3 um, n = 289. Collagen 10µg/ml, 7 um, n = 134; 5 um, n = 180; 3 um, n = 163. ICAM-1 10µg/ml, 7 um, n = 303; 5 um, n = 187; 3 um, n = 349. PLL-g-PEG 1mg/ml, 7 um, n = 145; 5 um, n = 55; 3 um, n = 117. Pluronic F-127 5% (w/v), 7 um, n = 167; 5 um, n = 62; 3 um, n = 181. Kruskal-Wallis test, ns not significant, * P < 0.05, *** P < 0.001.

Figure 3:

a: Migration of a neutrophil, pseudo colored by its aspect ratio, in a size-transition microchannel harboring a sharp narrowing from 6 µm to 3 µm width (4 µm height). b: Top, evolution of cell speed and cell aspect ratio over the x position in a size-transition microchannel. Position 0 corresponds to the necking. Bottom, fraction of cells displaying a speed increase, maintenance or decrease over the x axis, compared with the respective mean speed in the 6 µm wide section. Data are one representative of 5 experiments, n = 205 cells. c: Average speeds of 30 cells migrating from 6 µm to 3 µm wide section. d: Speed ratio: average speed in the 3 µm wide section normalized by the average speed in the 6 µm wide section. Each light dot represents a cell, and dark dot represents a median of one experiment. From five independent experiment, n = 544 cells. e: Crossing time or time spent in the necking (see bottom drawing figure 3a). Each light dot represents a cell, and dark dots represent a median of one experiment. From five independent experiment, n = 544 cells. f: Image of a microchannel with successive transition between 6 µm and 3 µm widths. g: Migratory behavior of neutrophils in a successive size-transition microchannel. Top, cell speed and cell aspect ratio over the x position in a successive size-transition microchannel. Transitions from 6 µm to 3 µm are indicated with dotted vertical lines. Bottom, fraction of cells displaying a speed increase, maintenance or decrease over the x axis, compared with the respective mean speed in the first 6 µm wide section. Data are one representative of 2 experiments, n = 159 cells. h: Crossing times for three consecutive transitions (6 µm to 3 µm wide section). Dots, individual cells. From five independent experiment, T1, n=

128 cells, T2, n = 139 cells, T3= 109 cells. i: Image of a tapered microchannel with gradual confinement from 8 µm to 3 µm width. j: Migratory behavior of neutrophils in a funnel microchannel, transitioning gradually from 8 to 3 µm width. Top, cell speed and cell aspect ratio over the x position in a funel microchannel of 300 µm length (left) or 600 µm length (right). Bottom, fraction of cells displaying a speed increase, maintenance or decrease over the x axis. Data are one representative of 2 and 3 experiments (300 and 600 µm length respectively). L = 300 µm, n = 21 cells. L = 600 µm, n = 19 cells. k: Migratory behaviors of immature dendritic cells (iDCs), T-Lymphocytes (TL) and natural killer cells (NK) in a size-transition microchannel. Top, cell speed and cell aspect ratio over the x position in a size-transition microchannel. Position 0 corresponds to the necking. Bottom, fraction of cells displaying a speed increase, maintenance or decrease over the x axis, compared with the respective mean speed in the 6 µm wide section. Data are one representative of 3 (iDC), 2 (TL) and 2 (NK) experiments, iDCs, n = 79 cells; TL, n = 38 cells; NK, n = 56 cells. l: Speed ratio of iDC, TL and NK cells in size-transition microchannels. Dots, individual cells. iDCs, n = 79 cells; TL, n = 38 cells; NK, n = 56 cells. In b, g, j, k bins size is indicated by the bar length and the sliding window is indicated by the shift between the two bars (upper left).

Figure 4:

a: Kimograph of a Lifeact-EGFP expressing neutrophil migrating in size-transition microchannel. Each row represents a timepoint (30 seconds). Lifeact-EGFP intensity is represented in inverted gray color. b: Magnification of the timepoints indicated by * in 1a. The cell is migrating toward the right in 6 µm wide (top) and 3 µm wide section (bottom). c: Average Lifeact-EGFP intensity of n = 348 cells migrating from 6 µm to 3 µm wide section. Data pooled from 4 independent experiments. d: Drawing explaining the quantification of neutrophil Back to Front Actin Ratio (BFAR) e: Mean BFAR of individual neutrophils in the 6 µm and 3 µm wide section. Light dots, individual cells, n = 348 cells. Dark dots, BFAR medians of 4 independent experiments. Wilcoxon test (paired), **** $P < 0.0001$. f: Top, BFAR and cell aspect ratio over the x position in a size-transition microchannel. Position 0 corresponds to the necking. Bottom, fraction of cells over the x axis, with BFAR values between indicated BFAR ranges. Data are one representative of 4 experiments, n = 50 cells. g: Scatter plot showing the correlation between BFAR ratio and speed ratio. Ratios are defined by the mean values in 3 µm section divided by mean values of 6 µm

section for individual cells. Speed decrease/increase are indicated with colored rectangles. Spearman correlation coefficient = 0.5880, P < 0.0001. h: Average Lifeact-EGFP intensity mapping of migrating neutrophils in straight microchannels of different widths. Data are 60 cells per channel width, from 3 independent experiments (20 cells per experiment). i: Kimographs of Lifeact-EGFP expressing neutrophils migrating in 6 µm wide (left) and 3 µm wide straight microchannels for 50 seconds. Lifeact-EGFP intensity is represented in inverted gray color. j: Mean BFAR of migrating neutrophils in straight microchannels of different widths. Data are pooled from 4 independent experiments. Light dots, individual cells; dark dots, median of experiment. 8 µm, n = 216; 7 µm, n = 210; 6 µm, n = 256; 5 µm, n = 289; 4 µm, n = 271, 3 µm, n = 253. Kruskall-Wallis test. ns = not significant; *** P < 0.001; **** P < 0.0001. k: Proportion of cells with mean BFAR below or above 1. From n = 4 independent experiments. l: Relation between BFAR and cell speed of neutrophils migrating in 6 µm and 3 µm wide straight microchannels. Light dots, instantaneous timepoint; dark dots, mean of individual cells. Data are one representative of 4 independent experiments.

Figure 5:

a: Immunostaining of Phospho-Myosin Light Chain (P-MLC) of fixed neutrophils in 6 µm and 3 µm wide microchannels. Ten cells are represented. P-MLC level is in inverted gray. b: P-MLC levels per cell area. Data are normalized by the average P-MLC level in the 6 µm wide microchannel of each experiment. Data are pooled from 3 independent experiments; 6 µm, n = 54 cells; 3 µm, n = 92 cells. Mann Whitney test, P < 0.0001. c: Kimograph of a MyoII-GFP expressing neutrophil migrating in size-transition microchannel. Data represent the signal in the middle cross-section of the cell obtained with spinning disk confocal microscope. d: Cortical MyoII-GFP intensity of 3 timepoints indicated in c. e: Evolution of cortical MyosinIIA-GFP intensity and cell aspect ratio over time of neutrophils migrating in a size-transition microchannel. Data are pooled from n = 15 cells of 2 independent experiments. Time 0 and vertical dotted line indicate the time at which the cell front starts to enter in the 3 µm wide section. Cortical signal is normalized to the total MyoII-GFP signal of the cell. f: Average speeds of cells migrating from 6 µm to 3 µm wide section, treated or not with Blebbistatin (25 µM) or Y-27632 (25 µM). Data are pooled from 3 (BBS) and 4 (Y-27632) independent experiments. DMSO, n = 196 cells; BBS, n =188 cells; H20, n = 376 cells, Y-27632, n = 231 cells. Mann Whitney test, P < 0.0001. g: Speed

ratio of neutrophils treated or not with BBS (25 µM), Y-27632 (25 µM) or ML-7 (20µM). Each light dot represents a cell, and dark dot represents a median of one experiment. Data are pooled from 3 (BBS), 4 (Y-27632) and 2 (ML-7) independent experiments. DMSO, n = 196 cells; BBS, n =188 cells; H20, n = 376 cells, Y-27632, n = 231 cells. DMSO (ML-7), n = 257; ML-7, n = 217. Mann Whitney test; ns, not significant; **** $P < 0.0001$. h: Crossing time of neutrophils treated or not with Y-27632 (25 µM). Data pooled from two independent experiments, CTR, n = 205; Y-27632, n = 97 cells. i: Kimograph of a Lifeact-EGFP expressing neutrophil treated with Y-27632 (25 µM) migrating in size-transition microchannel. Each row represents a timepoint (2 minutes). Lifeact-EGFP intensity is represented in inverted gray color. j: Top, speed and aspect ratio of Y-27632 treated neutrophils over the x position in a size-transition microchannel. Speed of the control condition is indicated in gray dotted line. Position 0 corresponds to the necking. Bottom, fraction of control and Y-27632 cells over the x axis, displaying a speed increase, maintenance or decrease over the x axis, compared with the respective mean speed in the 6 µm wide section. Data are one representative of 3 experiments, n = 95 cells. k: Top, BFAR of Y-27632 treated neutrophils (orange) and control cells (gray) over the x position in a size-transition microchannel. Bottom, fraction of control and Y-27632 cells over the x axis, with BFAR values between indicated BFAR ranges Data are one representative of 3 experiments, n = 95 cells. l: Average Lifeact-EGFP intensity of 60 control and Y-27632 treated cells migrating from 6 µm to 3 µm wide section. Data pooled from 3 independent experiments. m: Average Lifeact-EGFP intensity mapping of control and Y-27632 treated cells in straight microchannels of different widths. Data are 60 cells per channel width, from 2 independent experiments (20 cells per experiment).

Figure 6:

a: Kimograph of a Lifeact-EGFP expressing (stained with anti-Ly6G) neutrophil migrating in skin capillary. Each row represents a timepoint (30 seconds). Lifeact-EGFP intensity is represented in inverted gray color. Bottom, magnification of the timepoint indicated by *, cell contour in orange. b: Average Lifeact-EGFP intensity mapping of migrating neutrophils in skin capillaries. Data are n = 9 cells, from 1 experiment. c: Spinning disc-confocal images of liver sinusoids (gray, fluorescent BSA) and endogenous neutrophils (orange, Ly6G) 1 hour after LPS endotoxemia. Scale bar: 20 µm. d: Frequency distribution (percentage) of liver sinusoid diameters. Data are pooled from 4 independent experiments, for a total of 156 segments. e: Frequency distribution of

cell aspect ratio of neutrophils trafficking inside sinusoids. n=1119 shapes from 3 independent experiments. f: Migration speed of individual crawling cells in liver sinusoids, n = 72 cells from 3 independent experiments. g: Average Lifeact-EGFP intensity mapping of migrating neutrophils in skin capillaries. Data are 19 cells, from 2 experiments. h: Left, Kimograph of a Lifeact-EGFP expressing neutrophil migrating in liver sinusoid with a size-transition. Each row represents a timepoint (30 seconds), cell contour in red. Right, kymograph of the same cell color coded with aspect ratio value. i: Scatter plot of the relation between instantaneous BFAR and instantaneous cell speed of n = 9 cells (skin capillaries) and n = 19 cells (liver sinusoids). Spearman correlation coefficient (liver) = 0.39, $P < 0.0001$. Spearman correlation coefficient (skin) = 0.64, $P < 0.0001$.

MATERIALS AND METHODS

Mice

Male and female mice on a C57BL/6J (B6) genetic background were used at age ranging from 8 to 16 weeks. These mice were either wild-type (C53BBL/6J inbred strain, obtained from Charles Rivers) or genetically altered to express the Lifeact-EGP peptide (kind gift from M. Sixt)[54] or the Myosin IIA-GFP fusion protein (kind gift from R. S. Adelstein)[24]. These mouse strains did not exhibit a harmful phenotype thus their breeding and maintenance are not subjected to a project evaluation. Mice were housed under specific pathogen–free conditions within the animal research facility of the Institut Curie, in compliance with the European and French National Regulation for the Protection of Vertebrate Animals used for Experimental and other Scientific Purposes (Directive 2010/63; French Decree 2013-118). Mice were euthanized by cervical dislocation by appropriately qualified and trained individuals.

Intravital experiments

For intravital imaging, experiments were performed at Institut Pasteur in agreement with guidelines established by the French and European regulations for the care and use of laboratory animals and approved by the Institut Pasteur Committee on Animal Welfare (CETEA) under the protocol code CETEA 230080. C57BL/6 male and female mice were used at age ranging from 6 to 14 weeks and were housed under standard conditions (light 07.00–19.00 h; temperature 22 ± 1 °C; humidity 50 ± 10%) within the animal facility of the Institut Pasteur.

30-min prior to intravital imaging, mice were injected subcutaneously with buprenorphine (0.05 mg kg-1) and anesthetized by spontaneous inhalation of isoflurane in 100% oxygen (induction: 4%; maintenance: 1.5% at 0.3 L min−1). Mouse hydration and body temperature were respectively maintained by intraperitoneal injection of 200 µl 0.9% saline solution every hour and with 37 °C-heating pad. Labelling antibodies were injected intravenously 15min prior to imaging, 5µg of anti-Ly6G (clone 1A8) conjugated with Alexa-Fluor 488, 561 or 647 to label circulating neutrophils and 10 µg of CD31 (clone 390) conjugated with Alexa-Fluor 488, 561 or 647 to label the vasculature. Mice were imaged for up to 4 hours.

For infected dorsal back skin observations, mouse preparation was conducted as previously described[55]. Using Nanofill Syringe (World Precision Instruments), 3 intradermal injections of 1 µl of 10^8 CFU ml−1 bacterial suspension of the wild-type *N. meningitidis* strain were made[15]. For liver observations, organ preparation was conducted as previously described[56]. Mice were treated

with an intraperitoneal injection of 1 mg/kg purified LPS from E. coli 2-hours prior to intravital microscopy. For Lifeact-EGFP imaging in dorsal back skin and liver, purified bone-marrow Lifeact-EGFP expressing neutrophils (100 µl, $7.5x10^6$ cells) were injected intravenously 3-hour prior imaging.

Intravital imaging was performed using a Leica DM6 FS upright microscope equipped with a motorized stage. The microscope is fitted with HCX PL Fluotar 5x/0.15, HC Fluotar ×25/0.95 and HC PL APO ×40/ 1.10 objectives lens (Leica), mounted on an optical table to minimize vibration and totally enclosed in a biosafety cabinet (Noroit). The microscope is coupled to a Yokogawa CSU-W1 confocal head modified with Borealis technology (Andor). Four laser excitation wavelengths (488, 561, 642, and 730 nm) were used and visualized with the appropriate band-pass and long-pass filters. Fluorescence signals were detected using 2 sCMOS 2048 × 2048 pixels cameras (Orca Flash v2+, Hamamatsu) allowing simultaneous dual colors imaging. Metamorph acquisition software (Molecular devices) was used to drive the confocal microscope.

Mouse neutrophil isolation and culture

A single-cell suspension was prepared from mouse femur and tibia's bone marrow. Mouse neutrophils were isolated by immunomagnetic negative selection using the Mojosort neutrophil isolation kit (BioLegend, #480058) and according to the manufacturer's instructions. Expression of surface markers of neutrophils were analyzed by flow cytometry to assess the sample purity. Neutrophils enrichment was assessed by flow cytometry analysis of Ly6G and CD11b expression. After isolation, neutrophils were cultured overnight at a concentration of $1x10^6$ cells/mL in RPMI 1640 medium supplemented with fetal bovine serum (10 %), penicillin-streptomycin (100 U/mL) and recombinant granulocyte-macrophage colony-stimulating factor (GM-CSF, 50 ng/mL, Peprotech, #315-03-20UG).

Bone-marrow derived dendritic cells *in vitro* differentiation

The BMDCs were obtained by differentiation of bone marrow precursors for 10 days in IMDM-Glutamax medium supplemented with fetal bovine serum (10%), penicillin-streptomycin solution (100 U/ml), and β-mercaptoethanol (50 µM) and granulocyte-macrophage colony-stimulating factor (GM-CSF)-containing supernatant (50 ng/mL) obtained from transfected J558 cells, as previously described (Vargas, NCB). At day 10, semi-adherent cells were collected by carefully flushing with media after discarding the floating cells. Full differentiation was assessed by flow cytometry analysis of CD11c and CD80 expression.

Mouse T cell isolation, activation and expansion

Whole spleens were harvested from mice then dissociated in PBS into single-cell suspensions by passing the splenocytes through a sterile 70 µm mesh nylon strainers (Falcon, 352350). Naïve CD4+ T cells from mouse splenocytes were isolated by immunomagnetic negative selection, using the EasySep Mouse naïve CD4+ T Cell Isolation Kit (StemCell, # 19765). Isolated T cells were activated using monoclonal antibodies against the ε chain of mouse CD3 (subunit of the TCR complex) and the mouse CD28 co-stimulatory molecule for 24 hours and expanded in DMEM medium containing fetal bovine serum (10%), non-essential amino acids (1%), penicillin-streptomycin (100 U/mL), sodium pyruvate (1 mM), Beta-mercapto-ethanol (50 µM) and recombinant interleukine-2 (100U/mL, Preprotech, #212-12). T cells were used after 6 days of culture.

Mouse NK cell isolation and expansion

Fresh whole spleens were harvested from mice then dissociated in PBS into single-cell suspensions by passing the splenocytes through a sterile 70 µm mesh nylon strainers (Falcon, 352350). Subsequently, NK cells were enriched by negative selection with magnetic nanobeads using the MojoSort Mouse NK Cell Isolation Kit (Biolegend, cat. # 480050) according to the manufacturer's instructions. NK enrichment was assessed by flow cytometry analysis of NK1.1+/CD3- expressing cells. NK cells were cultured in 12-well flat-bottomed plates (Nest, cat. # 712001) at a concentration of $1x10^6$ cells/mL in culture media containing RPMI 1640 medium supplemented with FBS (10 %), non-essential amino acids (1 %), HEPES buffer, β-mercaptoethanol (55 µM), and recombinant interleukine-15 (7 nM, Biolegend, cat. # 566302). NK cells were used after 4-5 days of culture.

Photolithography

All microdevices used for this work were designed and prepared as follows. First, chrome photomasks were fabricated by JD photo Data (UK) from our designs with specific dimensions (negative pattern). Next, using photolithography technique, SI wafers were photopatterned with an SU-8 negative photoresist. The obtained Si wafers were subsequently silanized and a thick layer of PDMS (RTV615, Neyco) was poured over the wafer and cured at 65°C for at least 2h. PDMS was peeled off the Si wafer and used to prepare a replica mold using epoxy.

Microchannel preparation

Micro-channels experiments were performed as previously described (vargas et al). Briefly, A 10-to-1 mixture of PDMS (RTV615, Neyco) was poured into the custom-made epoxy molds. PDMS crosslinking was obtained after 2 hours at 65°C. PDMS chips were peeled off from the epoxy mold using a blade, cut at the edges, then 2- or 3-mm holes were drilled in the PDMS chamber in a region near the entry of microchannels, as a reservoir for cell loading. PDMS chamber and 35-mm glass-bottom dish (FD35-100, WPI) were cleaned then plasma activated before being bound to each other. The binding was left to strengthen in a 65 °C oven for 15 min.

For surface functionalization, the PDMS surfaces were plasma activated during 1 min and incubated with the coating solution at RT during 30 min. For most experiments, microchannels were coated with fibronectin (10 µg/ml, Sigma-Aldrich, #F1141). Alternatively, when specified, microchannels were coated with collagen (10µg/mL, Advanced BioMatrix, #5005), ICAM-1 (10µg/ml), pLL-PEG (1mg/ml) or Pluronic-F127 (50mg/ml). After the incubation step, PDMS chambers were washed three times with PBS then incubated with complete medium (containing drugs when specified) for 2 hours at 37 °C and 5% CO2 before cell loading.

Widefield time-lapse microscopy

For velocity measurements and actin imaging, migrating cells were recorded overnight with a DMi8 inverted microscope (Leica) at 37 ◦C with 5% CO2 atmosphere and a ×20 dry objective (NA 0.40 phase). One image every 30s during 6 h was recorded. The widefield microscope was controlled by MetaMorph software.

Spinning-disk time-lapse microscopy

For myosin imaging, migrating cells were recorded using a spinning-disc confocal microscope with a Yokogawa CSU-X1 spinning-disc head on a DMI-8 Leica inverted microscope equipped with a Hamamatsu OrcaFlash 4.0 Camera, a NanoScanZ piezo focusing stage (Prior Scientific) and a motorized scanning stage (Marzhauser). One slice with focus on the middle cell cross section was recorded every 5sec during for 1hour. The spinning-disk microscope was controlled by MetaMorph software (Molecular Devices) and equipped with an incubation chamber that maintained the temperature at 37°C and CO2 concentration at 5%.

Image processing

All images were exported from the Metamorph acquisition software (Molecular Devices) as .tiff files and edited using Fiji. Stacks were registered using Stackreg plugin or using SIFT multichannel plugin.

Image analysis

Three single-cell parameters (cell aspect ratio, cell speed, and F-actin intracellular distribution) were analyzed using in-house ImageJ macros. Briefly, kymographs for each microchannel (in each field of view) were generated using a semi-automated ImageJ macro. Individual cells migrating within the microchannels were segmented on each kymograph using a pixel classification algorithm (ilastik and Labkit, applied to the Lifeact-EGFP or MyoII-EGFP signal) to obtain a mask of the entire cell. The cell aspect ratio, used as a measure of cell deformation/elongation (Viridis LUT), was computed with ImageJ as the ratio of the major axis to the minor axis of the Feret ellipse approximating the cell. Instantaneous cell speed was determined by measuring the displacement of the cell centroid along the microchannel axis between two frames. The back-to-front actin ratio (BFAR) was calculated to evaluate intracellular F-actin distribution. The BFAR corresponds to the ratio of the mean F-actin fluorescence intensity measured in the rear half of the cell mask to that measured in the front half. A BFAR greater than 1 indicates an enrichment of F-actin at the rear of the cell, while a BFAR less than 1 indicates an enrichment of F-actin at the front of the cell.

Spatial analysis of single-cell parameters

The relative speed of cells migrating in microchannels with sharp transitions was calculated for each cell as the ratio of its instantaneous velocity to its average velocity in the first section of the microchannel. In microchannels with successive transitions, the average velocity of each cell was calculated in the first 6 µm section. In microchannels with a gradual narrowing, the relative speed of each cell was computed as the ratio of its instantaneous velocity to its average velocity.

To assess the evolution of BFAR, AR and speed along the x axis of the microchannels, we partitioned the x axis into fixed-size bins. Then, the average across cells in each bin was calculated. To avoid sampling bias and underrepresentation of the fastest cells, we partitioned the x axis into bins with a length equal to the largest cell displacement measured in the experiment. By doing so, each bin contains at least one measure for each cell. When more than one measure for a cell was recorded in a specific bin, these measures were averaged before the averaging across the cell population. Relative speed data and BFAR data were log2 transformed prior to the averaging across the cell population.

The crossing time between two microchannels sections was calculated as the time between the first cell contact with the narrowing section of the microchannel, and the time at which the whole cell was in the confined section.

Lifeact-EGFP density maps

Lifeact-EGFP density maps were generated as described (Vargas). Briefly, individual neutrophils migrating in microchannels were cropped using the ImageJ software. To map the Lifeact-EGFP signal, images of all timepoints of each individual cell were aligned in a single column. Cell size normalization was applied to each time point according to the mean cell size. To obtain the mean Lifeact-EGFP distribution of each cell, an average projection was performed on the t-stack. All cell average projections were then size-normalized and averaged to obtain the mean Lifeact-EGFP distribution of each condition.

Immunofluorescence

PDMS device (coated with fibronectin) with a transition from 6 x 4 µm (large) to 3 x 4 µm (narrow) channels were stick on 18 mm diameter glass coverslips. Neutrophils were prepared as mentioned above, plated in microchannels, and incubated for 2-3 hours at 37°C to let them migrate in large and narrow channels. Cells were fixed with 4% paraformaldehyde for 20 min at 37°C and washed with PBS. PDMS device was gently removed by first unsticking PDMS from coverslips with razor blades and then pulling vertically with tweezers. Cells were permeabilized with 0.1 % Triton X-100 for 10 min at room temperature, washed and blocked with PBS-BSA 3% overnight at 4°C. Cells were with stained with rabbit anti-pMLC (Cell Signaling Technology, 3674) for 24h at 4°C, washed, stained with a goat anti-rabbit AF647 (Invitrogen, A32733) for 1 hour at RT, and washed again. Cells were stained for 5 min with DAPI (Ref) and the coverslip was mounted on a glass slide with Fluoromount G (Molecular probes). Images were taken with the spinning-disc confocal microscope, with a 40X objective (Ref). Z stacks of 20 slices every 0.5 µm were taken. Image analysis was performed using ImageJ/Fiji software (NIH, https://rsb.info.nih.gov/ij/index.html). ROIs of single cells in 6 x4 µm or 3 x 4 µm channels were cropped. Z max projection of Phalloidin signal was used for cell segmentation, and P-MLC mean intensity was measured within cell area at each slice for every cells. We kept the 5 slices with the maximum P-MLC mean intensity and calculated the average intensity within these 5 slices. For images presented in (Figure 5a), z max projection of P-MLC signal of the 5 slices were represented, with cell contours (from cell segmentation).

Immunoblotting

500k cells were first treated in suspension with Y-27632 25µM for 30 min (Supplementary Figure 5b). Cells were washed with cold PBS and resuspended in RIPA buffer for 30 min. Protein lysates were mixed with Laemmeli buffer. Proteins were separated using polyacrylamide gel electrophoresis (NuPAGE Bis-Tris gels, 4%–12%, Invitrogen) and transferred onto nitrocellulose membranes (iBlot™ Transfer Stacks, Invitrogen) using iBlot Western Blot Transfer System (Invitrogen). Membranes were blocked with 5% BSA in Tris-buffered saline containing 0.05% Tween (TBS-Tween) for 1 h at room temperature, after which primary antibodies were added in TBS-Tween 5% BSA and incubated over night at 4°C. The membranes were washed (3 x 10 min) in TBS-Tween after which secondary horseradish peroxidase conjugated antibodies (Jackson ImmunoResearch) were added in 5% BSA in TBS-Tween and incubated for 1 h at room temperature. After extensive washing (3 x 10 min) in TBS-Tween, ECL signal was recorded on a ChemiDoc Touch Biorad Imager.

REFERENCES

1. Kolaczkowska, E. & Kubes, P. Neutrophil recruitment and function in health and inflammation. *Nat. Rev. Immunol.* **13**, 159–175 (2013).
2. Lämmermann, T. *et al.* Neutrophil swarms require LTB4 and integrins at sites of cell death in vivo. *Nature* **498**, 371–375 (2013).
3. Wang, J. *et al.* Visualizing the function and fate of neutrophils in sterile injury and repair. *Science* **358**, 111–116 (2017).
4. Nourshargh, S., Hordijk, P. L. & Sixt, M. Breaching multiple barriers: leukocyte motility through venular walls and the interstitium. *Nat. Rev. Mol. Cell Biol.* **11**, 366–378 (2010).
5. Brown KA, Treacher DF. Neutrophils as potential therapeutic targets in sepsis. (2006).
6. Manley, H. R., Keightley, M. C. & Lieschke, G. J. The Neutrophil Nucleus: An Important Influence on Neutrophil Migration and Function. *Front. Immunol.* **9**, (2018).
7. Calì, B. *et al.* Atypical CXCL12 signaling enhances neutrophil migration by modulating nuclear deformability. *Sci. Signal.* **15**, eabk2552 (2022).
8. Prentice-Mott, H. V. *et al.* Biased migration of confined neutrophil-like cells in asymmetric hydraulic environments. *Proc. Natl. Acad. Sci.* **110**, 21006–21011 (2013).
9. Wang, X., Hossain, M., Bogoslowski, A., Kubes, P. & Irimia, D. Chemotaxing neutrophils enter alternate branches at capillary bifurcations. *Nat. Commun.* **11**, 2385 (2020).
10. Sormendi, S. *et al.* HIF2α is a direct regulator of neutrophil motility. *Blood* **137**, 3416–3427 (2021).
11. Reversat, A. *et al.* Cellular locomotion using environmental topography. *Nature* **582**, 582–585 (2020).
12. Doerschuk, C. M. Mechanisms of Leukocyte Sequestration in Inflamed Lungs. *Microcirculation* **8**, 71–88 (2001).
13. Cruz Hernández, J. C. *et al.* Neutrophil adhesion in brain capillaries reduces cortical blood flow and impairs memory function in Alzheimer's disease mouse models. *Nat. Neurosci.* **22**, 413–420 (2019).
14. Dholakia, K. Y., Guevara-Torres, A., Feng, G., Power, D. & Schallek, J. In Vivo Capillary Structure and Blood Cell Flux in the Normal and Diabetic Mouse Eye. *Invest. Ophthalmol. Vis. Sci.* **63**, 18 (2022).
15. Harding, M. G., Zhang, K., Conly, J. & Kubes, P. Neutrophil Crawling in Capillaries; A Novel Immune Response to Staphylococcus aureus. *PLoS Pathog.* **10**, e1004379 (2014).
16. Bogoslowski, A. *et al.* Neutrophils Recirculate through Lymph Nodes to Survey Tissues for Pathogens. *J. Immunol.* ji2000022 (2020) doi:10.4049/jimmunol.2000022.
17. McDonald, B. *et al.* Intravascular Danger Signals Guide Neutrophils to Sites of Sterile Inflammation. *Science* **330**, 362–366 (2010).
18. Rolfes, L. *et al.* Neutrophil granulocytes promote flow stagnation due to dynamic capillary stalls following experimental stroke. *Brain. Behav. Immun.* **93**, 322–330 (2021).
19. El Amki, M. *et al.* Neutrophils Obstructing Brain Capillaries Are a Major Cause of No-Reflow in Ischemic Stroke. *Cell Rep.* **33**, 108260 (2020).

20. Erdener, Ş. E. *et al.* Dynamic capillary stalls in reperfused ischemic penumbra contribute to injury: A hyperacute role for neutrophils in persistent traffic jams. *J. Cereb. Blood Flow Metab.* **41**, 236–252 (2021).
21. Ng, L. G., Ostuni, R. & Hidalgo, A. Heterogeneity of neutrophils. *Nat. Rev. Immunol.* **19**, 255–265 (2019).
22. Paluch, E. K., Aspalter, I. M. & Sixt, M. Focal Adhesion–Independent Cell Migration. *Annu. Rev. Cell Dev. Biol.* **32**, 469–490 (2016).
23. Wilson, K. *et al.* Mechanisms of leading edge protrusion in interstitial migration. *Nat. Commun.* **4**, 2896 (2013).
24. Zhang, Y. *et al.* Mouse models of MYH9-related disease: mutations in nonmuscle myosin II-A. *Blood* **119**, 238–250 (2012).
25. Lomakin, A. J. *et al. The Nucleus Acts as a Ruler Tailoring Cell Responses to Spatial Constraints*. http://biorxiv.org/lookup/doi/10.1101/863514 (2019) doi:10.1101/863514.
26. Venturini, V. *et al.* The nucleus measures shape changes for cellular proprioception to control dynamic cell behavior. *CELL Biol.* 13 (2020).
27. Srivastava, N., Traynor, D., Piel, M., Kabla, A. J. & Kay, R. R. Pressure sensing through Piezo channels controls whether cells migrate with blebs or pseudopods. *Proc. Natl. Acad. Sci.* **117**, 2506–2512 (2020).
28. Amano, M., Nakayama, M. & Kaibuchi, K. Rho-Kinase/ROCK: A Key Regulator of the Cytoskeleton and Cell Polarity. *Cytoskelet. Hoboken Nj* **67**, 545–554 (2010).
29. Renkawitz, J. *et al.* Nuclear positioning facilitates amoeboid migration along the path of least resistance. *Nature* **568**, 546–550 (2019).
30. Moreau, H. D. *et al.* Macropinocytosis Overcomes Directional Bias in Dendritic Cells Due to Hydraulic Resistance and Facilitates Space Exploration. *Dev. Cell* **49**, 171-188.e5 (2019).
31. Barbier, L. *et al.* Myosin II Activity Is Selectively Needed for Migration in Highly Confined Microenvironments in Mature Dendritic Cells. *Front. Immunol.* **10**, 747 (2019).
32. Wang, X. *et al.* Progressive mechanical confinement of chemotactic neutrophils induces arrest, oscillations, and retrotaxis. *J. Leukoc. Biol.* **0**,.
33. Ruef, N. *et al.* Exocrine gland–resident memory $CD8^+$ T cells use mechanosensing for tissue surveillance. *Sci. Immunol.* **8**, eadd5724 (2023).
34. Saez, A. *et al.* Lamin A/C and the Immune System: One Intermediate Filament, Many Faces. *Int. J. Mol. Sci.* **21**, 6109 (2020).
35. Rowat, A. C. *et al.* Nuclear Envelope Composition Determines the Ability of Neutrophil-type Cells to Passage through Micron-scale Constrictions. *J. Biol. Chem.* **288**, 8610–8618 (2013).
36. Vargas, P. *et al.* Innate control of actin nucleation determines two distinct migration behaviours in dendritic cells. *Nat. Cell Biol.* **18**, 43–53 (2016).
37. Leithner, A. *et al.* Diversified actin protrusions promote environmental exploration but are dispensable for locomotion of leukocytes. *Nat. Cell Biol.* **18**, 1253–1259 (2016).
38. Keller, H., Zadeh, A. D. & Eggli, P. Localised depletion of polymerised actin at the front of Walker carcinosarcoma cells increases the speed of locomotion. 14.

39. Tsai, T. Y.-C. *et al.* Efficient Front-Rear Coupling in Neutrophil Chemotaxis by Dynamic Myosin II Localization. *Dev. Cell* **49**, 189-205.e6 (2019).
40. Chabaud, M. *et al.* Cell migration and antigen capture are antagonistic processes coupled by myosin II in dendritic cells. *Nat. Commun.* **6**, 7526 (2015).
41. Lavi, I., Piel, M., Lennon-Duménil, A.-M., Voituriez, R. & Gov, N. S. Deterministic patterns in cell motility. *Nat. Phys.* **12**, 1146–1152 (2016).
42. Bretou, M. *et al.* Lysosome signaling controls the migration of dendritic cells. *Sci. Immunol.* **2**, eaak9573 (2017).
43. Sáez, P. J. *et al.* ATP promotes the fast migration of dendritic cells through the activity of pannexin 1 channels and P2X7 receptors. *Sci. Signal.* **10**, eaah7107 (2017).
44. Sakamoto, R., Izri, Z., Shimamoto, Y., Miyazaki, M. & Maeda, Y. T. Geometric trade-off between contractile force and viscous drag determines the actomyosin-based motility of a cell-sized droplet. *Proc. Natl. Acad. Sci.* **119**, e2121147119 (2022).
45. Aoun, L. *et al.* Leukocyte transmigration and longitudinal forward-thrusting force in a microfluidic Transwell device. *Biophys. J.* **120**, 2205–2221 (2021).
46. Liu, Y.-J. *et al.* Confinement and Low Adhesion Induce Fast Amoeboid Migration of Slow Mesenchymal Cells. *Cell* **160**, 659–672 (2015).
47. Balzer, E. M. *et al.* Physical confinement alters tumor cell adhesion and migration phenotypes. *FASEB J.* **26**, 4045–4056 (2012).
48. Hung, W.-C. Confinement Sensing and Signal Optimization via Piezo1/PKA and Myosin II Pathways. 13.
49. Böhringer, D. *et al.* Dynamic traction force measurements of migrating immune cells in 3D biopolymer matrices. *Nat. Phys.* (2024) doi:10.1038/s41567-024-02632-8.
50. Brunet, T. *et al.* A flagellate-to-amoeboid switch in the closest living relatives of animals. *eLife* **10**, e61037 (2021).
51. Ju, R. J. *et al.* Compression-dependent microtubule reinforcement enables cells to navigate confined environments. *Nat. Cell Biol.* **26**, 1520–1534 (2024).
52. Kopf, A. *et al.* Microtubules control cellular shape and coherence in amoeboid migrating cells. *J. Cell Biol.* **219**, e201907154 (2020).
53. Meyers, J., Craig, J. & Odde, D. J. Potential for Control of Signaling Pathways via Cell Size and Shape. *Curr. Biol.* **16**, 1685–1693 (2006).
54. Riedl, J. *et al.* Lifeact mice for studying F-actin dynamics. *Nat. Methods* **7**, 168–169 (2010).
55. Manriquez, V. *et al.* Colonization of dermal arterioles by Neisseria meningitidis provides a safe haven from neutrophils. *Nat. Commun.* **12**, 4547 (2021).
56. Dal-Secco, D. *et al.* A dynamic spectrum of monocytes arising from the in situ reprogramming of CCR2+ monocytes at a site of sterile injury. *J. Exp. Med.* **212**, 447–456 (2015).

Figure 1

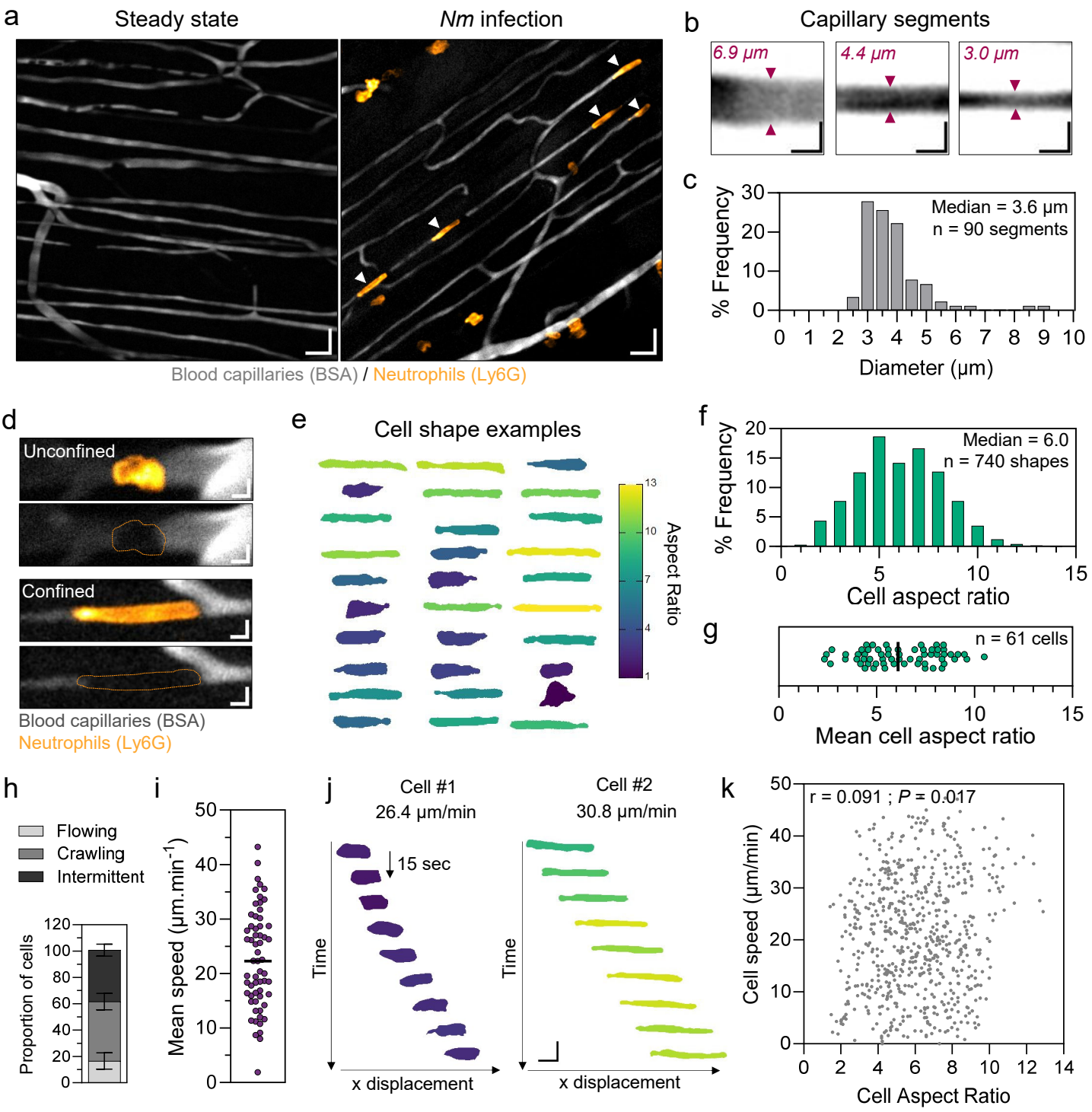
a
Steady state
Nm infection
Blood capillaries (BSA) / Neutrophils (Ly6G)
b
Capillary segments
6.9 µm
4.4 µm
3.0 µm
c
% Frequency
Median = 3.6 µm
n = 90 segments
Diameter (µm)
d
Unconfined
Confined
Blood capillaries (BSA)
Neutrophils (Ly6G)
e
Cell shape examples
Aspect Ratio
f
% Frequency
Median = 6.0
n = 740 shapes
Cell aspect ratio
g
n = 61 cells
Mean cell aspect ratio
h
Flowing
Crawling
Intermittent
Proportion of cells
i
Mean speed (µm.min-1)
j
Cell #1
26.4 µm/min
15 sec
Time
x displacement
Cell #2
30.8 µm/min
Time
x displacement
k
r = 0.091 ; P = 0.017
Cell speed (µm/min)
Cell Aspect Ratio

Figure 2

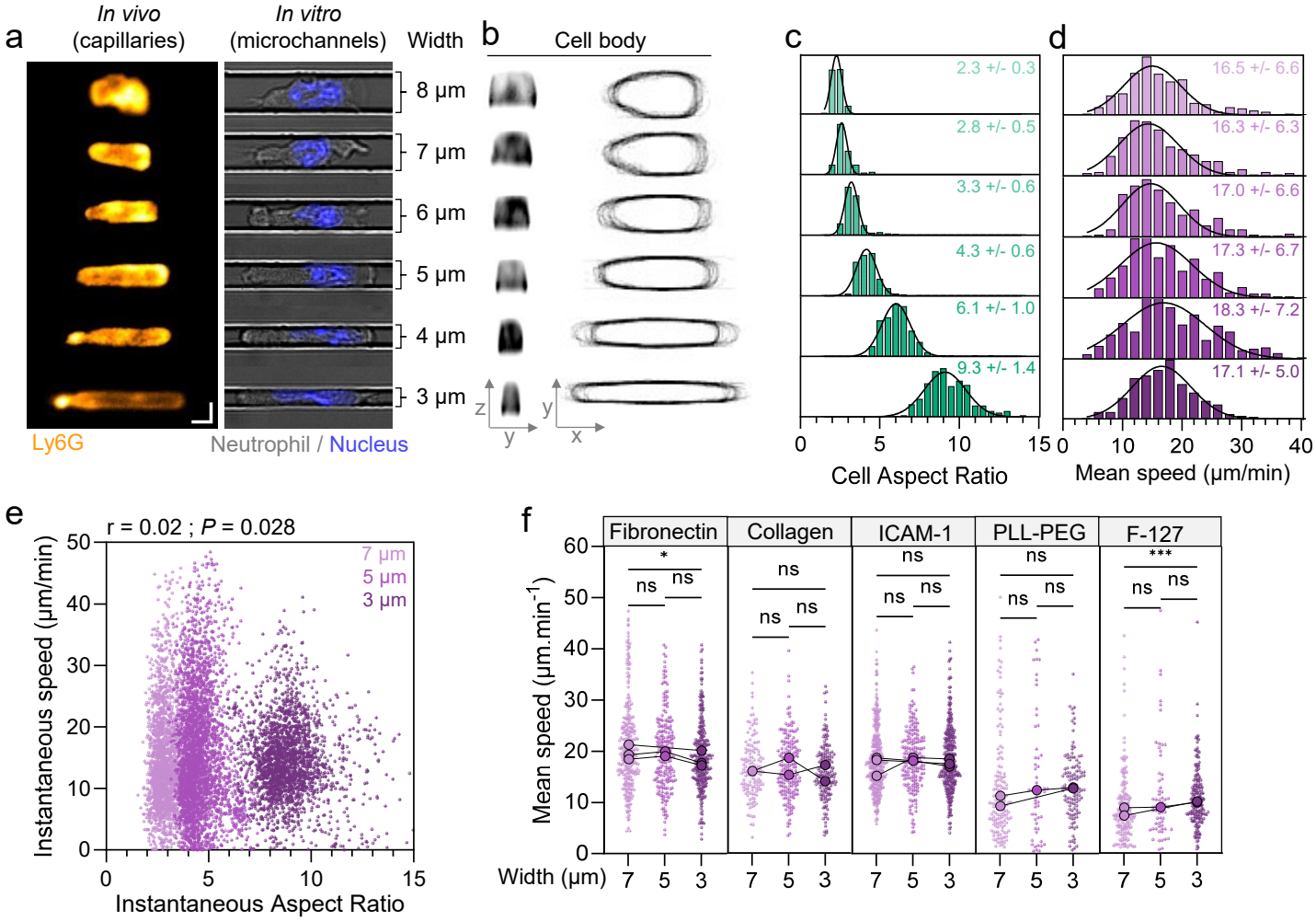
a
In vivo
(capillaries)
In vitro
(microchannels)
Width
8 µm
7 µm
6 µm
5 µm
4 µm
3 µm
Ly6G
Neutrophil / Nucleus
b
Cell body
z
y
y
x
c
2.3 +/- 0.3
2.8 +/- 0.5
3.3 +/- 0.6
4.3 +/- 0.6
6.1 +/- 1.0
9.3 +/- 1.4
0
5
10
15
Cell Aspect Ratio
d
16.5 +/- 6.6
16.3 +/- 6.3
17.0 +/- 6.6
17.3 +/- 6.7
18.3 +/- 7.2
17.1 +/- 5.0
0
10
20
30
40
Mean speed (µm/min)
e
r = 0.02 ; P = 0.028
7 µm
5 µm
3 µm
Instantaneous speed (µm/min)
Instantaneous Aspect Ratio
f
Fibronectin
Collagen
ICAM-1
PLL-PEG
F-127
Mean speed (µm.min-1)
Width (µm)
ns
*
***

Figure 3

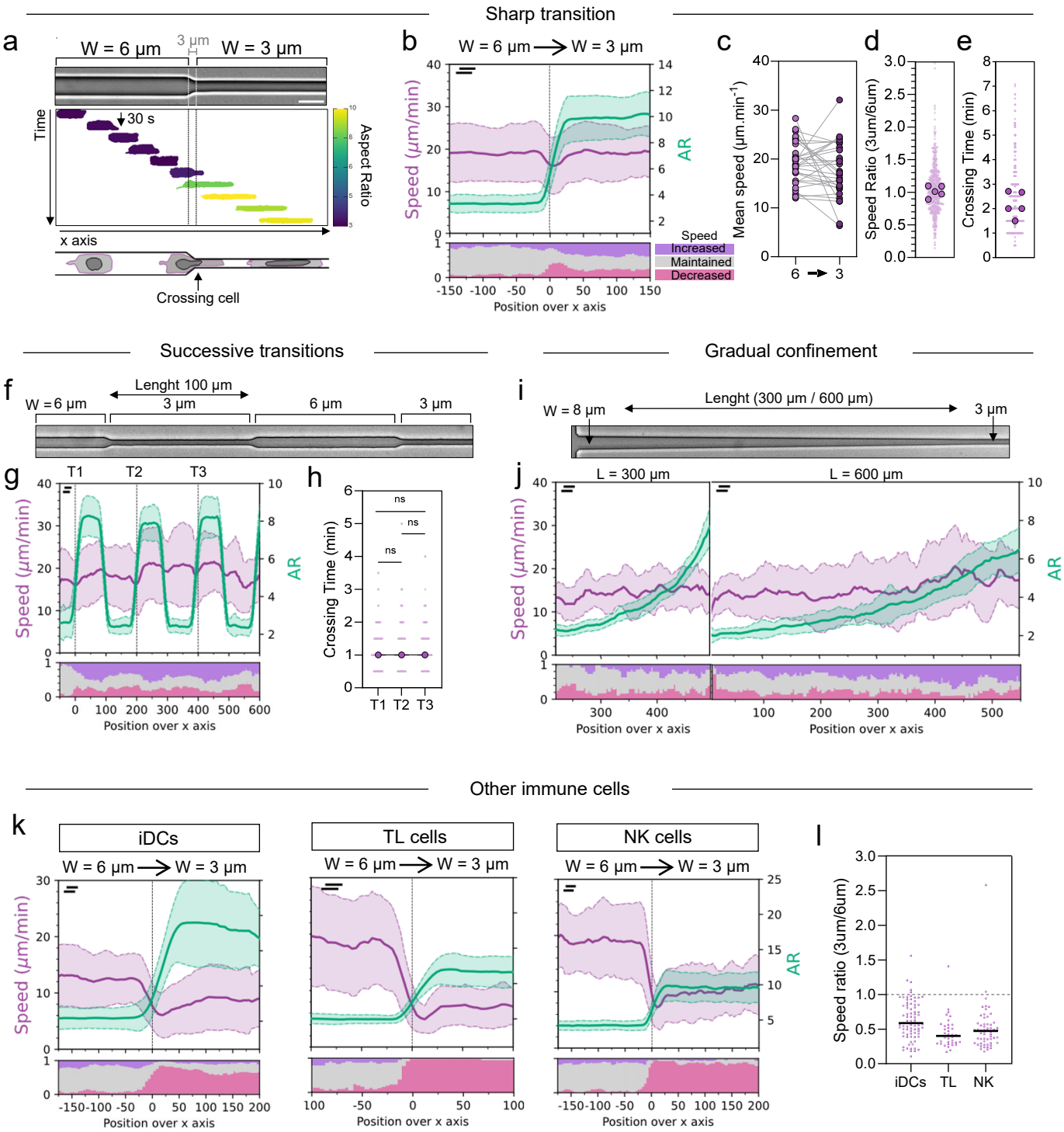
Sharp transition
a
W = 6 µm
3 µm
W = 3 µm
Time
30 s
Aspect Ratio
x axis
Crossing cell
b
W = 6 µm → W = 3 µm
Speed (µm/min)
AR
Speed
Increased
Maintained
Decreased
Position over x axis
c
Mean speed (µm.min⁻¹)
6 → 3
d
Speed Ratio (3um/6um)
e
Crossing Time (min)
Successive transitions
f
W = 6 µm
Lenght 100 µm
3 µm
6 µm
3 µm
g
T1
T2
T3
Speed (µm/min)
AR
Position over x axis
h
Crossing Time (min)
ns
ns
ns
T1 T2 T3
Gradual confinement
i
W = 8 µm
Lenght (300 µm / 600 µm)
3 µm
j
L = 300 µm
L = 600 µm
Speed (µm/min)
AR
Position over x axis
Position over x axis
Other immune cells
k
iDCs
TL cells
NK cells
W = 6 µm → W = 3 µm
W = 6 µm → W = 3 µm
W = 6 µm → W = 3 µm
Speed (µm/min)
AR
Position over x axis
Position over x axis
Position over x axis
l
Speed ratio (3um/6um)
iDCs
TL
NK

Figure 4

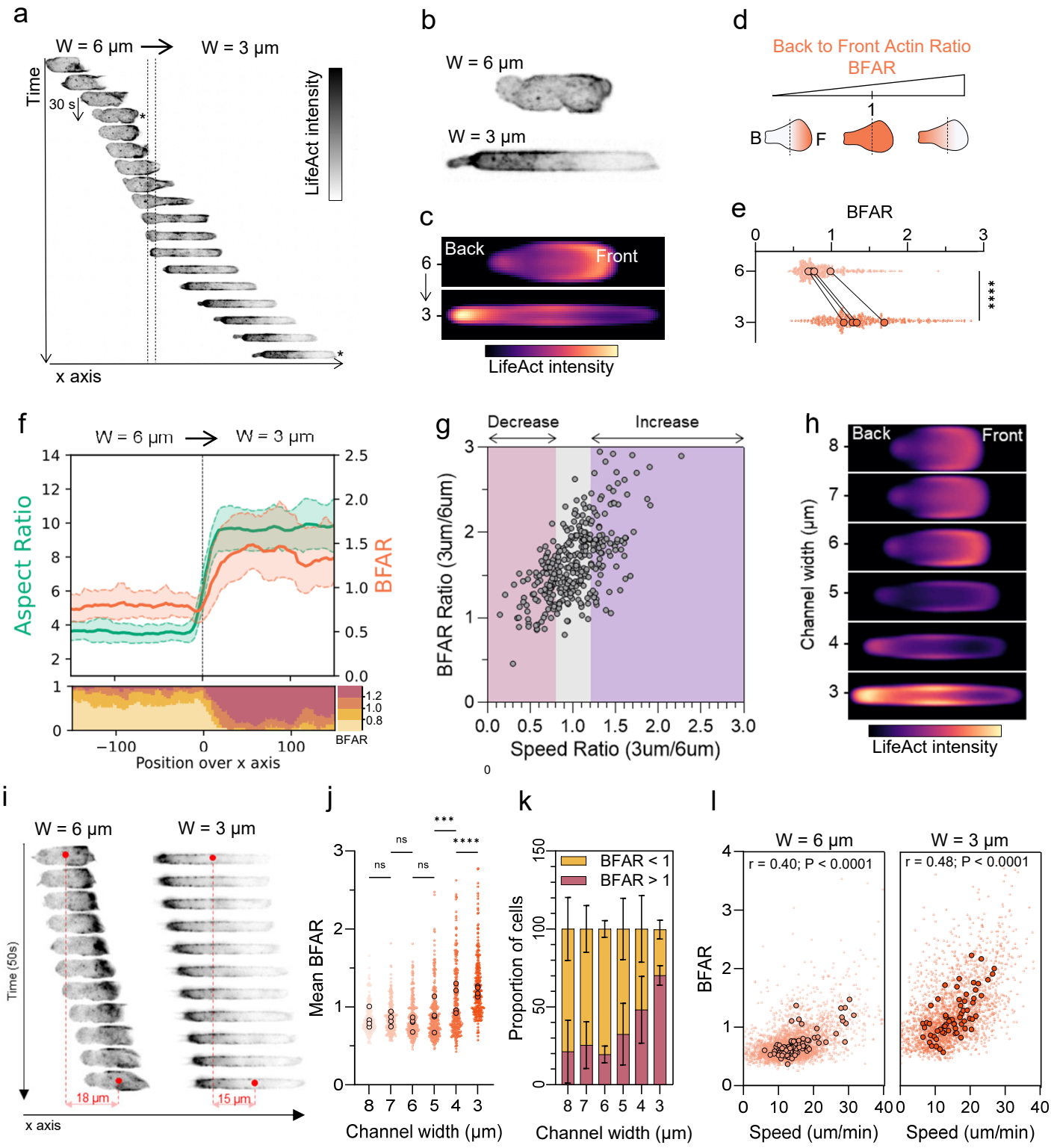
a
W = 6 µm
W = 3 µm
Time
30 s
LifeAct intensity
x axis
b
W = 6 µm
W = 3 µm
c
Back
Front
6
3
LifeAct intensity
d
Back to Front Actin Ratio
BFAR
1
B
F
e
BFAR
0
1
2
3
6
3
****
f
W = 6 µm
W = 3 µm
Aspect Ratio
BFAR
Position over x axis
g
Decrease
Increase
BFAR Ratio (3um/6um)
Speed Ratio (3um/6um)
h
Back
Front
Channel width (µm)
LifeAct intensity
i
W = 6 µm
W = 3 µm
Time (50s)
18 µm
15 µm
x axis
j
Mean BFAR
ns
ns
ns
***
****
Channel width (µm)
k
BFAR < 1
BFAR > 1
Proportion of cells
Channel width (µm)
l
W = 6 µm
W = 3 µm
r = 0.40; P < 0.0001
r = 0.48; P < 0.0001
BFAR
Speed (um/min)
Speed (um/min)

Figure 5

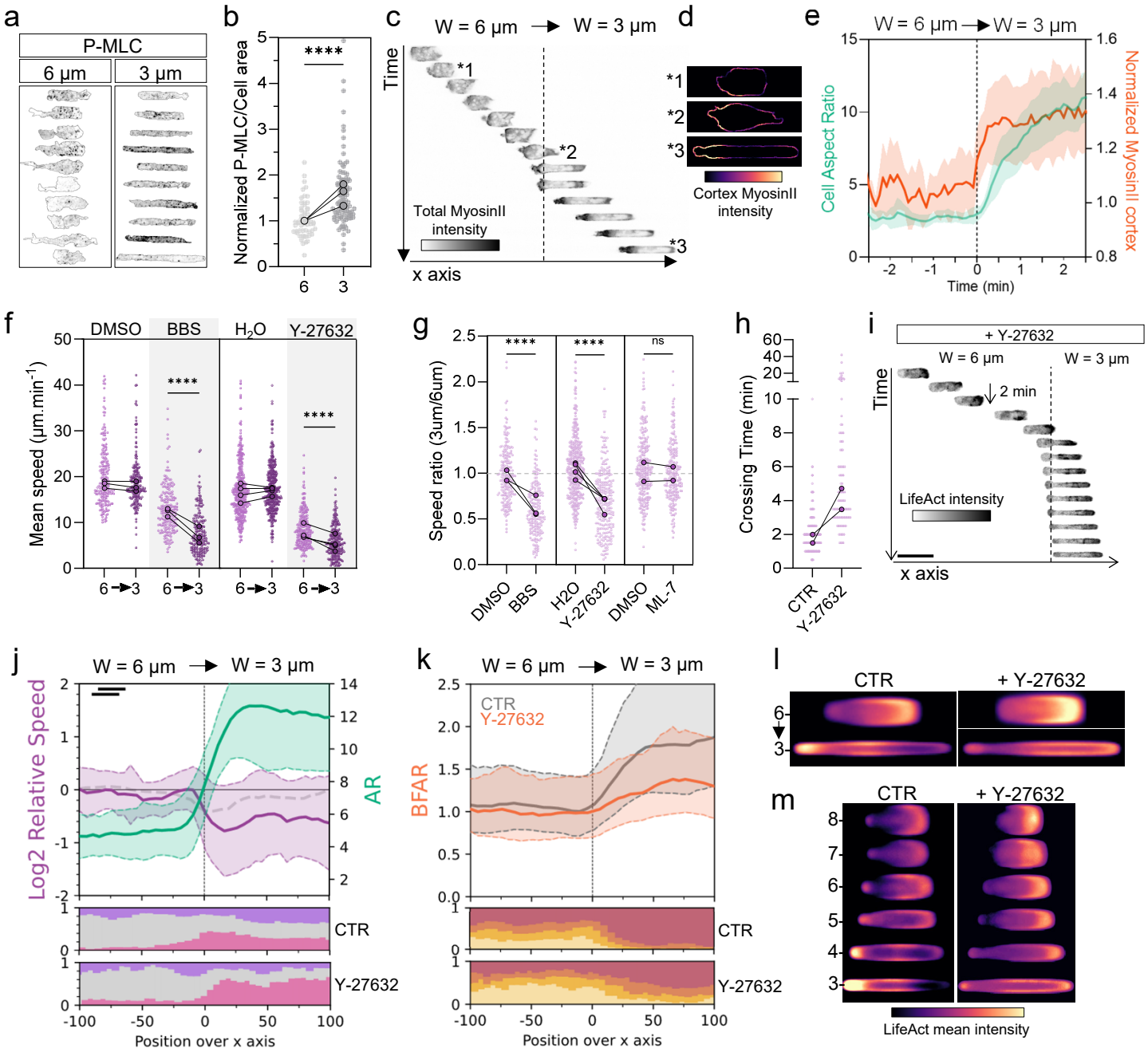
a
P-MLC
6 µm
3 µm
b
Normalized P-MLC/Cell area
****
6
3
c
W = 6 µm → W = 3 µm
Time
*1
*2
*3
Total MyosinII intensity
x axis
d
*1
*2
*3
Cortex MyosinII intensity
e
W = 6 µm → W = 3 µm
Cell Aspect Ratio
Normalized MyosinII cortex
Time (min)
f
DMSO
BBS
H2O
Y-27632
Mean speed (µm.min-1)
****
****
6→3
g
Speed ratio (3um/6um)
****
****
ns
DMSO
BBS
H2O
Y-27632
DMSO
ML-7
h
Crossing Time (min)
CTR
Y-27632
i
+ Y-27632
W = 6 µm
W = 3 µm
Time
2 min
LifeAct intensity
x axis
j
W = 6 µm → W = 3 µm
Log2 Relative Speed
AR
CTR
Y-27632
Position over x axis
k
W = 6 µm → W = 3 µm
CTR
Y-27632
BFAR
CTR
Y-27632
Position over x axis
l
CTR
+ Y-27632
6
3
m
CTR
+ Y-27632
LifeAct mean intensity

Figure 6

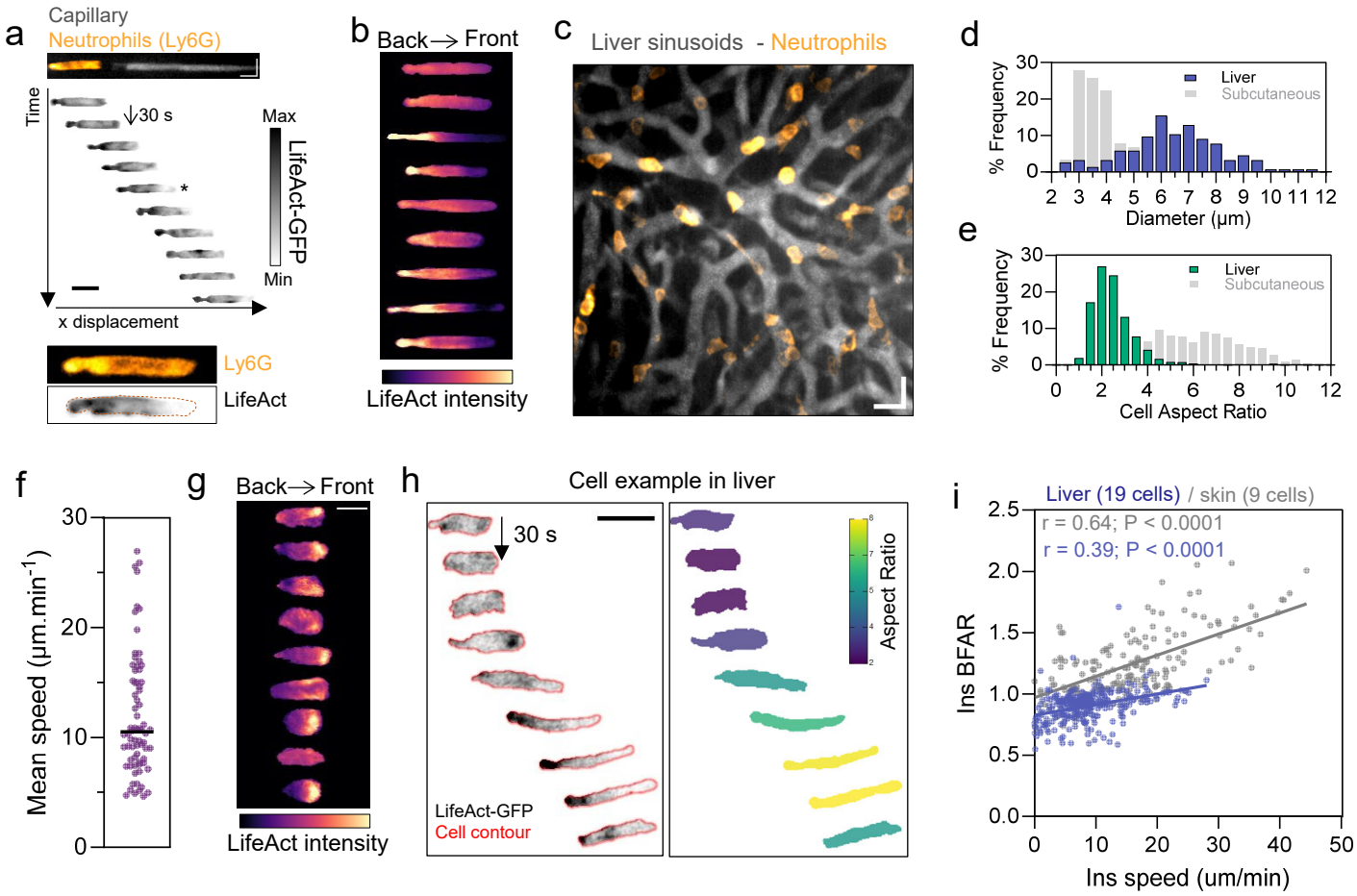
a
Capillary
Neutrophils (Ly6G)
Time
30 s
Max
LifeAct-GFP
Min
x displacement
Ly6G
LifeAct
b
Back→ Front
LifeAct intensity
c
Liver sinusoids - Neutrophils
d
% Frequency
Liver
Subcutaneous
Diameter (µm)
e
% Frequency
Liver
Subcutaneous
Cell Aspect Ratio
f
Mean speed (µm.min-1)
g
Back→ Front
LifeAct intensity
h
Cell example in liver
30 s
LifeAct-GFP
Cell contour
Aspect Ratio
i
Liver (19 cells) / skin (9 cells)
r = 0.64; P < 0.0001
r = 0.39; P < 0.0001
Ins BFAR
Ins speed (um/min)

Supplementary - Figure 1

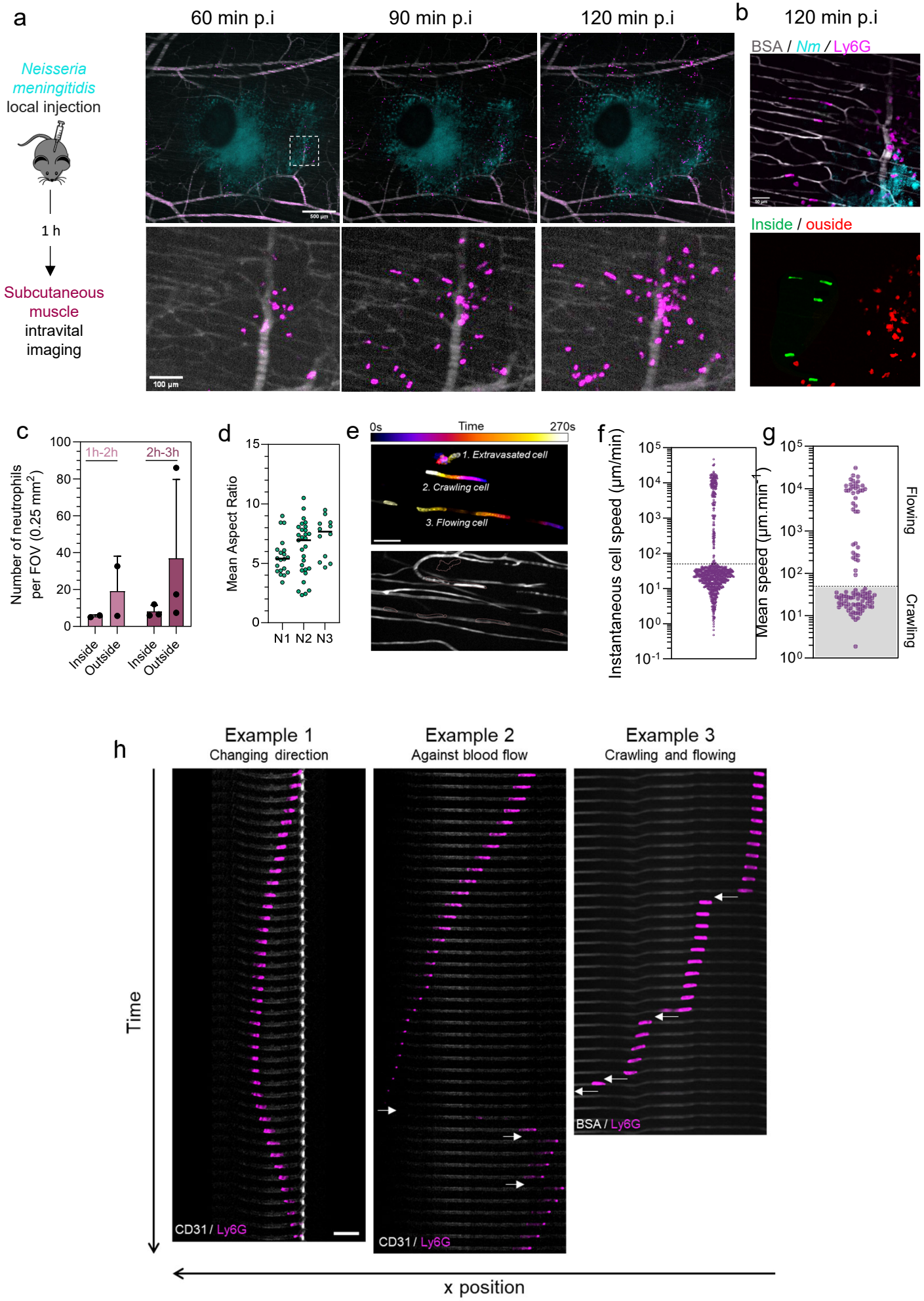

Supplementary - Figure 2

a

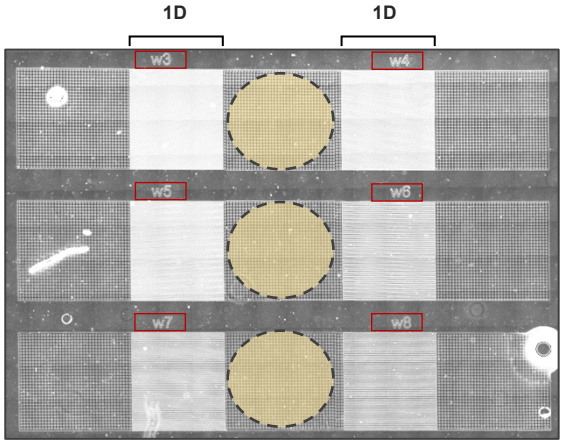

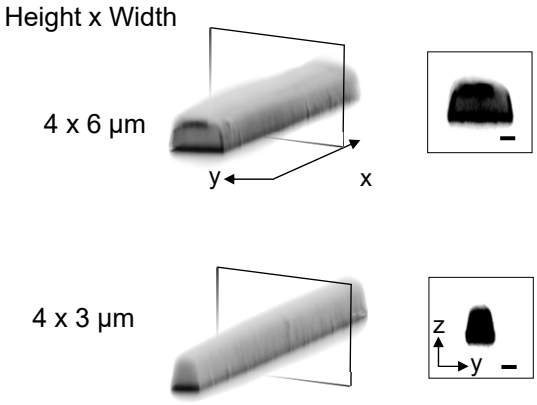

b

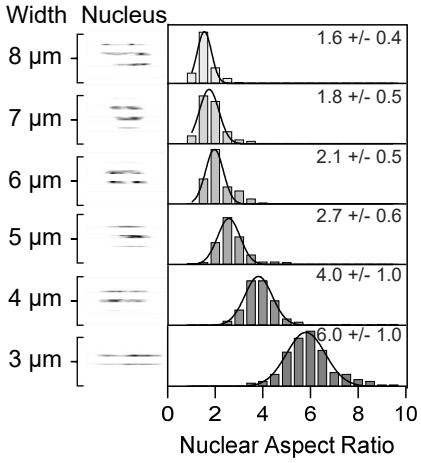

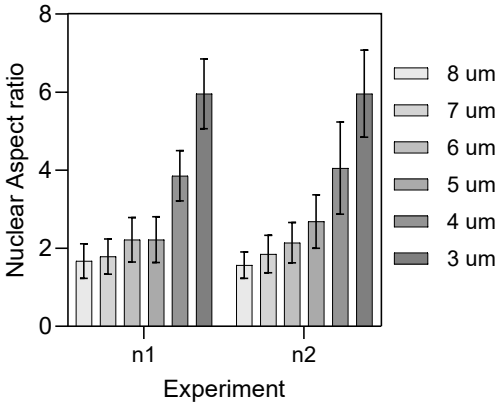

c

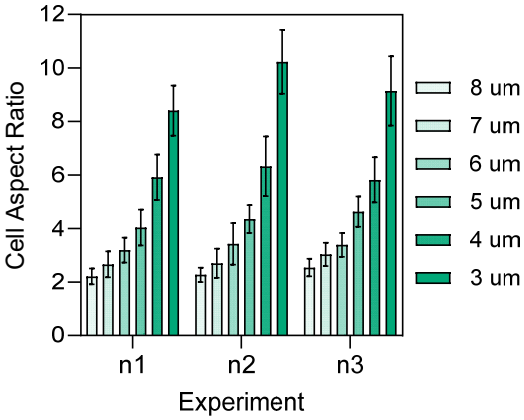

d

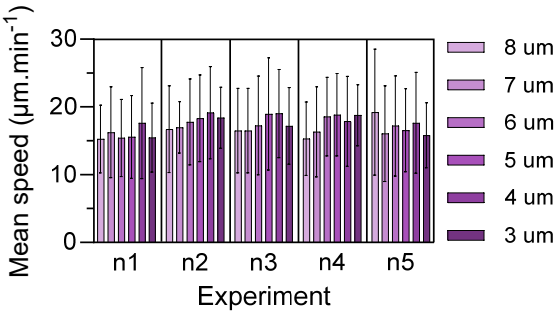

Supplementary Figure 3

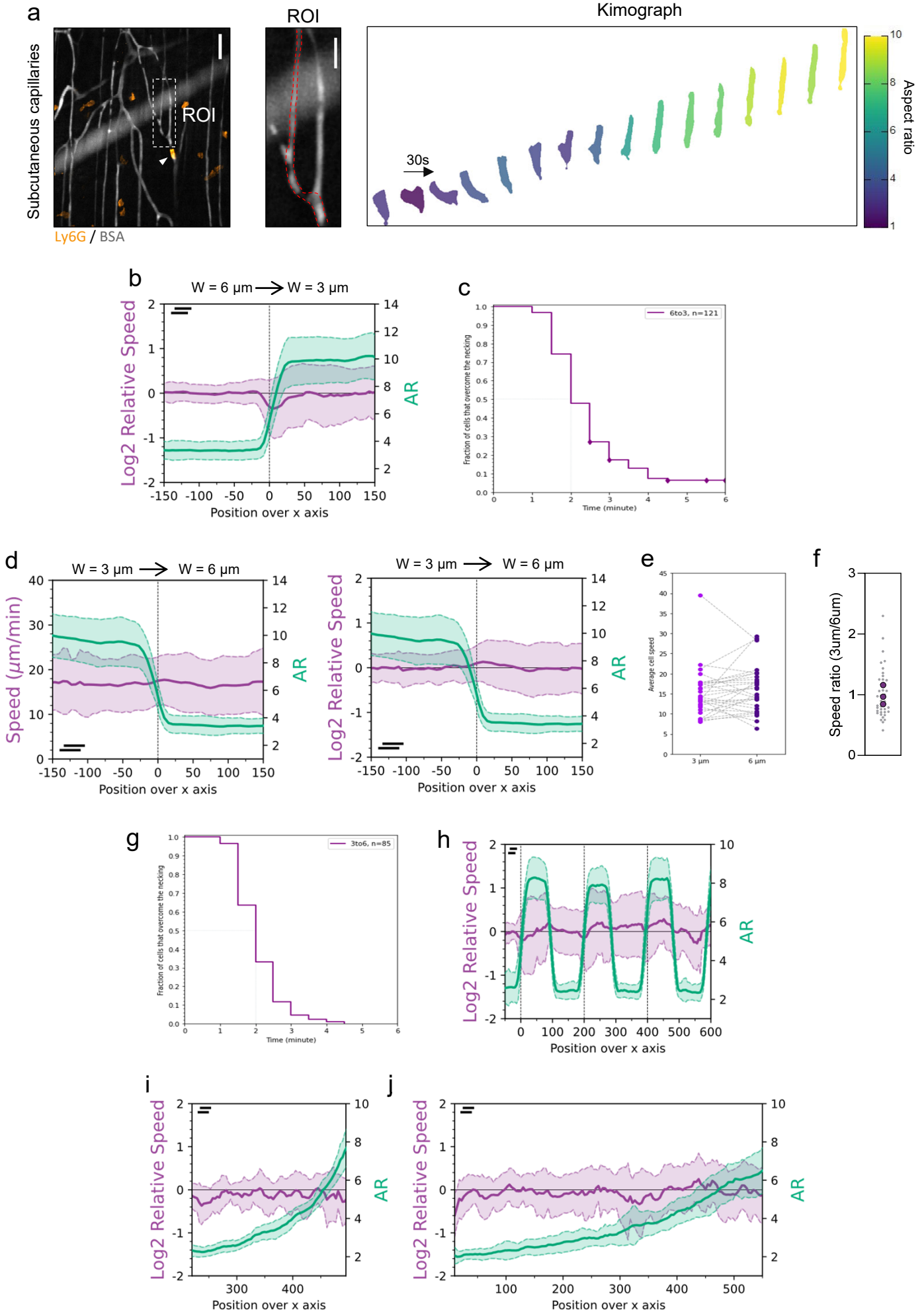

Figure 4 - supplementary

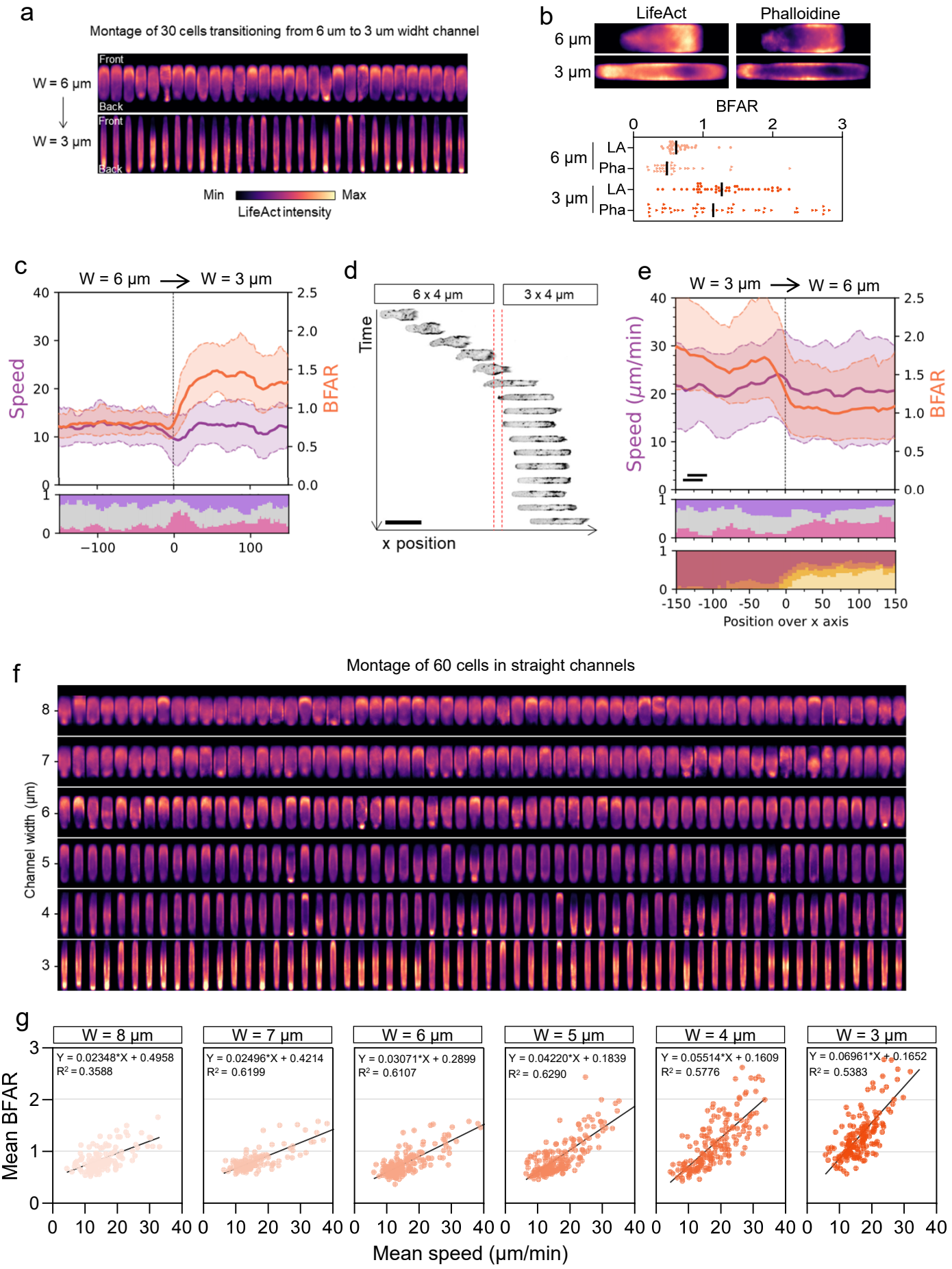

Figure 5 - supplementary

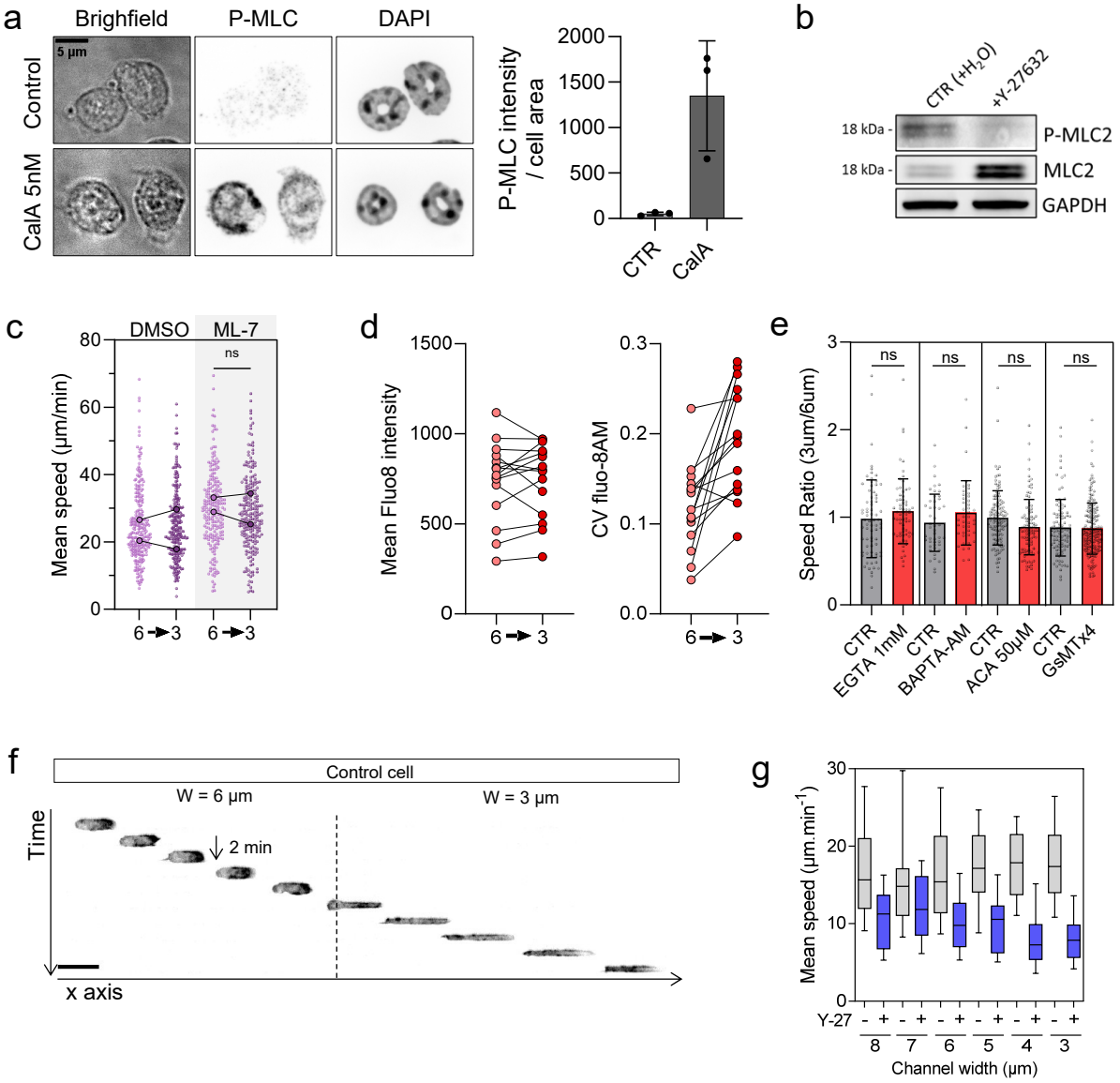

Figure 6 - supplementary

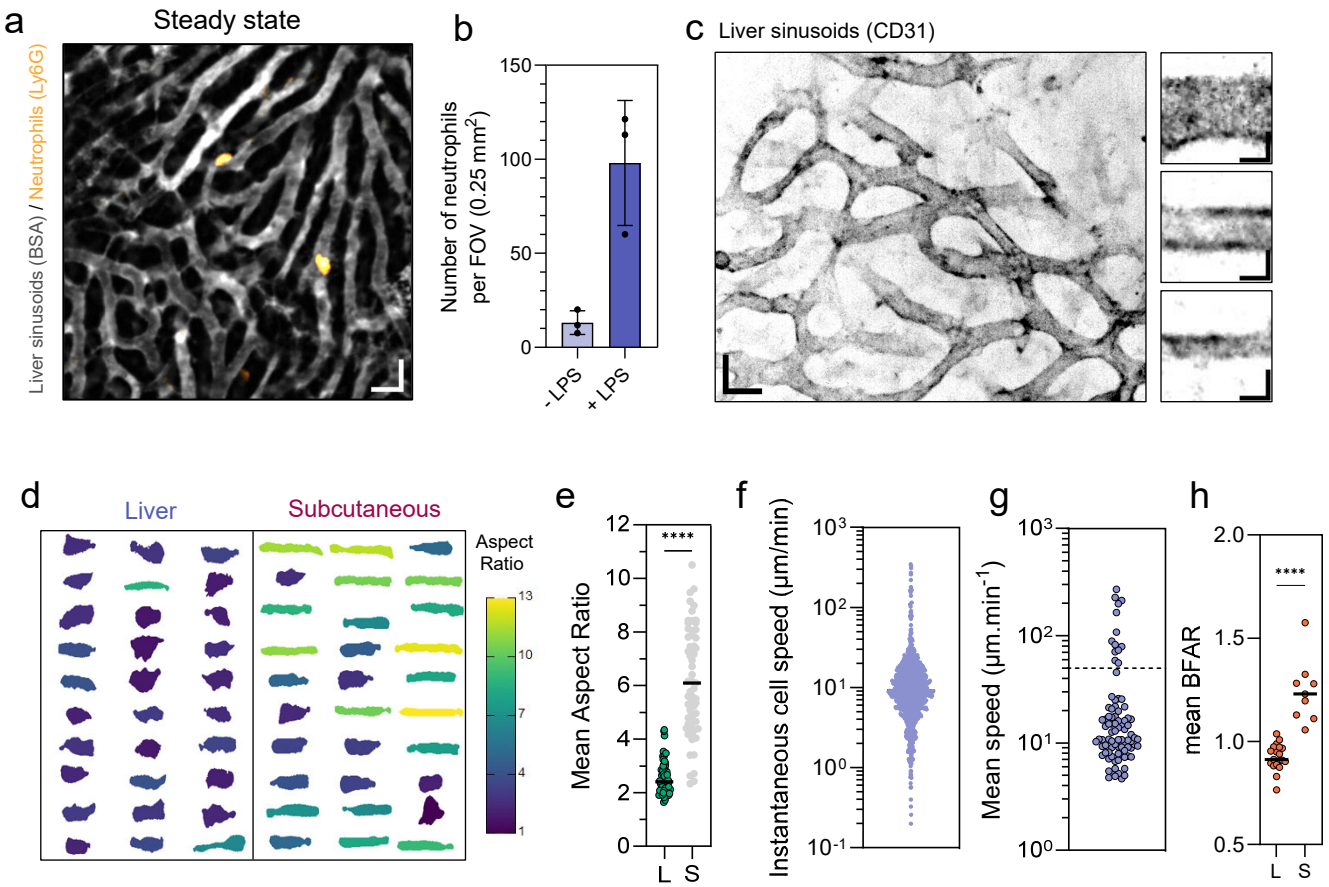
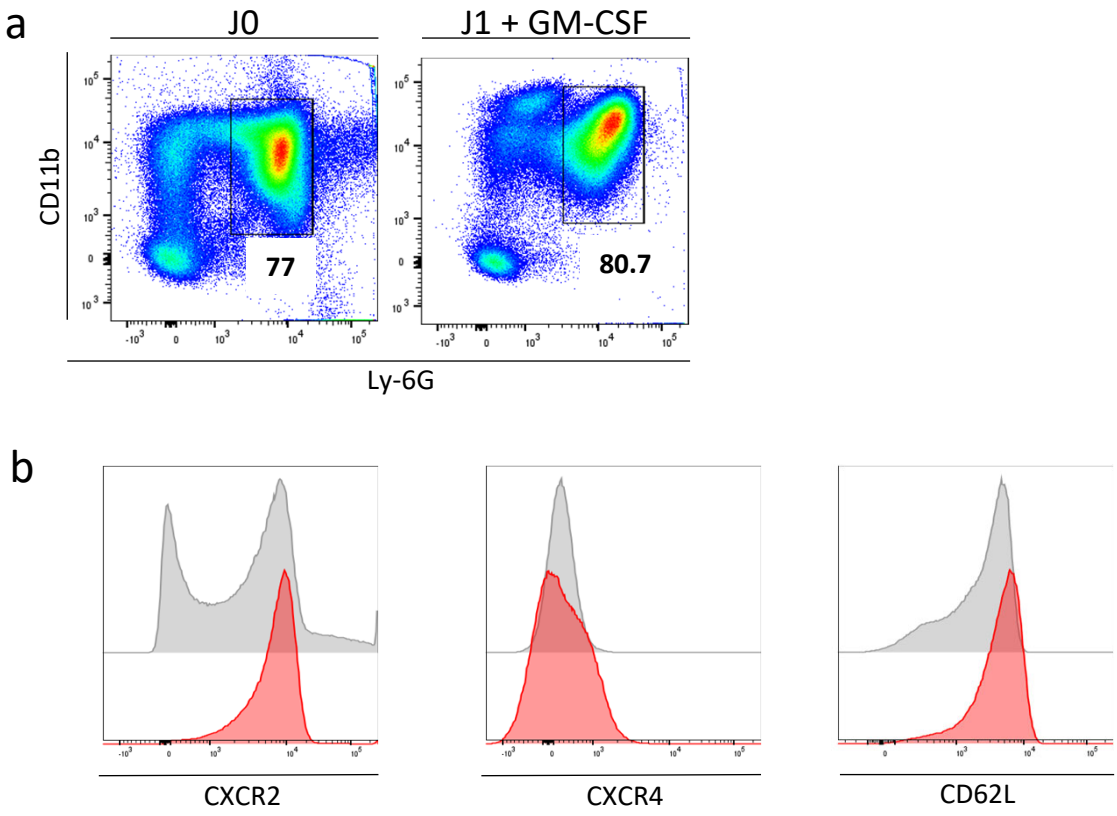
Figure 7 - supplementary